

# Introducing a Harmonic Balance Navier-Stokes Finite Element Solver to Accelerate Cardiovascular Simulations

Dongjie Jia and Mahdi Esmaily

November 22, 2024

## Abstract

The adoption of cardiovascular simulations for diagnosis and surgical planning on patient-specific basis requires development of faster methods than the existing state-of-the-art techniques. To address this need, we leverage the periodic nature of these flows to accurately capture their time-dependence using spectral discretization. Owing to the reduced size of the discrete problem, the resulting approach, known as the harmonic balance method, significantly lowers the cost of solution when compared against the conventional time marching methods. This study describes a stabilized finite element implementation of the harmonic balanced method that targets simulation of physically-stable time-periodic flows. That stabilized method is based on the Galerkin/least-squares formulation that permits stable solution in convection-dominant flows and convenient use of same interpolation functions for velocity and pressure. We test this solver against its equivalent time marching method using three common physiological cases where blood flow is modeled in a Glenn operation, a cerebral artery, and a left main coronary artery. Using the conventional time marching solver, simulating these cases takes more than ten hours. That cost is reduced by up to two orders of magnitude when the proposed harmonic balance solver is utilized, where a solution is produced in approximately 30 minutes. We show that that solution is in excellent agreement with the conventional solvers when the number of modes is sufficiently large to accurately represent the imposed boundary conditions.

## 1 Introduction

Computational Fluid Dynamics (CFD) has played a foundational role in studying cardiovascular blood flows in the recent decades [1, 2, 3, 4]. These simulations provide a non-invasive way of accessing information that is difficult or impossible to obtain using conventional clinical methods. Simulation results such as flow paths, pressure distribution, and wall shear stress can provide critical information for non-invasive diagnosis [5, 6, 7, 8], predictive surgical planning [9, 10, 11], and surgical optimisation [12, 13, 14]. Unfortunately, the applications are mainly limited to research settings due to the cost of performing high-accuracy simulations, which ranges from hours to days when run on a dedicated computing cluster [15, 16]. Such cost can become a limiting factor in real-life patient-specific settings considering the availability of computational resources and the short time frame available for clinical decision-making.

One current cost-saving strategy for CFD simulation in clinical settings involves assuming steady-state flows. Simulating transient cardiovascular flows is a resource-intensive process, which requires repeatedly solving millions of degrees of freedom for thousands of time steps each cardiac cycle for multiple cycles to reach solution convergence. When the steady-state assumption is used instead of transient analysis, the required number of time steps is significantly reduced, which in turn reduces the simulation cost. An example in practice is calculating fractional flow reserve (FFR) to analyze coronary artery disease, which takes minutes to compute the steady-state CFD result [17, 18, 19, 20]. However, because the steady-state assumption does not capture the cardiovascular system's dynamic and pulsatile behavior, the results carry significant errors compared to measured FFR values. Furthermore, steady-state CFD cannot provide estimations for transient-dependent parameters, such as maximum wall shear stress and pressure. Other strategies use modeling to circumvent performing CFD in clinical settings and eliminate the computation cost associated with simulations. These modeling techniques, such as reduced order modeling [21, 22, 23, 24],

and more recently, data-driven machine learning [25, 26, 27], uses prior obtained CFD results or clinical data to construct data-informed models. Although these models are cost-efficient for clinical use, they struggle to accommodate patient-specific variations in conditions and geometries. In addition, these models do not yield high resolution three-dimensional temporal-spacial results like CFD. They also do not fundamentally satisfy fluid conservation laws, making their hemodynamic predictions error-prone. Therefore, transient CFD remains the gold standard for accurate patient-specific cardiovascular simulations.

As mentioned above, conventional transient CFD simulation uses time-stepping to advance the solution in time. The time-stepping scheme is responsible for a large portion of the simulation cost due to the significant number of time steps required per cardiac cycle and multiple cycles to achieve converged periodic results. On the other hand, the periodic and smooth temporal behavior of physically stable cardiovascular flows can be well-approximated using a few frequency modes. Solving those selective frequency modes can reduce the simulation cost significantly compared to the conventional time-stepping scheme. In a recent series of studies, we suggested conducting transient cardiovascular CFD simulations in the time-spectral (or frequency) domain [28, 29, 30, 31]. The implementation of the frequency finite element solver requires several innovative approaches, starting with a specialized code structure to separate the complex values to use only real arithmetics in the solver and a pressure stabilization scheme to allow equal shape functions for pressure and velocity [28, 29]. In addition, a new finite element stabilization method was proposed to improve solution accuracy and compared against other existing stabilization methods in solving the frequency convection-diffusion equation [30].

The stabilized finite element method is widely used for cardiovascular simulations due owing to its ability to handle complex geometries, unstructured grid, and fluid-structure interaction [32, 33, 34, 35]. In our latest published work, we developed a CFD solver that uses a specialized stabilized finite element method to solve the Navier-Stokes equation in frequency domain [31]. The frequency solver’s requirements are identical to a conventional CFD solver, given boundary conditions and a volumetric mesh. Our results showed that the frequency solver provided accurate outlet flow rate and pressure results within 5% of a conventional CFD solver while significantly reducing simulation time. However, the frequency solver’s simulation cost scales quadratically with the number of simulated frequency modes. This cost scaling diminishes the cost-saving benefits of the frequency solver when a large number of frequency modes is needed for a simulation.

In this study, we will use the harmonic balance method to resolve the cost-scaling issue of the frequency solver. The harmonic balance method is a frequency domain method used to calculate the response of an unsteady nonlinear system without the need for time integration. [36] It is most widely used for simulating strong nonlinear behaviors such as mechanical vibration and nonlinear electrical circuits [37, 38]. For fluid dynamics applications, harmonic balance CFD simulations have been utilized in aerospace and turbomachinery studies using the finite volume and the finite difference methods [39, 40, 41, 42, 43, 44, 45]. The use of the harmonic balance method for simulating cardiovascular flow has not been thoroughly explored [46]. In this paper, we use the harmonic balance form of the Navier-Stokes equations as proposed in a previous paper [47]. This form of the equations is a direct transform of the frequency Navier-stokes equations used in our previous study [31]. The harmonic balance form has the advantage of using only real-valued variables and allows for approximately linear cost-scaling with the number of frequency modes. Solving this form of equations results in considerably lower computation costs when a large number of frequency modes is simulated.

This paper represents the first instance of combining the harmonic balance method with the stabilized finite element method to solve the Navier-Stokes equations. Using the proposed harmonic balance finite element solver, we will simulate three different cardiovascular cases with patient-specific anatomy: a Glenn procedure pulmonary flow, a cerebral flow, and a coronary artery flow. Subsequently, we will compare the results with those obtained from a conventional time-stepping CFD solver. These cases hold unique clinical significance and hemodynamic flow patterns and will serve as compelling examples to showcase the effectiveness of the proposed harmonic balance solver. We aim to demonstrate that the proposed solver is ready for application in various physiological cases, thereby paving the way for its potential use in future studies. The paper is organized as follows: we will first introduce the derivation of the harmonics-balance Navier-Stokes equation and present the stabilized finite element method. Next, we will provide comprehensive details about the solution procedure to solve the system of equations. We will present results obtained from the three cardiovascular cases and use them to demonstrate the harmonic balance solver’s cost and accuracy compared to the conventional solver. Finally, we will discuss the implications of the results, the existing

limitations, and potential future work.

## 2 Methods

This section will outline the numerical methods used to create the harmonic balance CFD solver. We will present the derivation of the harmonic balance form of the Navier-Stokes equations. We will then present the stabilized finite element weak form utilized in this study and briefly discuss other stabilization methods. Finally, we will present the solution procedure for solving the resulting system of equations to achieve optimal speed and cost scaling. This section will provide sufficient details for readers to adapt an existing conventional finite element solver to solve the harmonic balance Navier-Stokes equations.

### 2.1 Harmonic balance Navier-Stokes equations

In this study, we will solve the incompressible flow assumption since we are solving blood flow. We also consider blood as Newtonian since the length scale of the major blood vessels is significantly larger than the size of a red blood cell. We are also only considering stationary walls. Further research is needed to apply this method to solve fluid-structure interactions.

With these assumptions, the three-dimensional incompressible Navier-Stokes equation in the Cartesian coordinate system and the time domain is formulated as

$$\begin{aligned}
\rho \frac{\partial \hat{u}_i}{\partial t} + \rho \hat{u}_j \frac{\partial \hat{u}_i}{\partial x_j} &= -\frac{\partial \hat{p}}{\partial x_i} + \frac{\partial}{\partial x_j} \left( \mu \frac{\partial \hat{u}_i}{\partial x_j} \right), & \text{in } \Omega \times (0, N_c T] \\
\frac{\partial \hat{u}_i}{\partial x_i} &= 0, & \text{in } \Omega \times (0, N_c T] \\
\hat{u}_i &= \hat{g}_i, & \text{on } \Gamma_g \times (0, N_c T] \\
-\hat{p} n_i + \mu \frac{\partial \hat{u}_i}{\partial x_j} n_j &= \hat{h} n_i, & \text{on } \Gamma_h \times (0, N_c T]
\end{aligned} \tag{1}$$

where subscripts  $i$  and  $j$  denotes the spatial orientation where  $i, j = 1, 2, 3$ .  $\rho \in \mathbb{R}^+$  and  $\mu \in \mathbb{R}^+$  are the fluid density and dynamic viscosity, respectively, and  $\hat{u}_i(\mathbf{x}, t) \in \mathbb{R}$  and  $\hat{p}(\mathbf{x}, t) \in \mathbb{R}$  are the unknown fluid velocity and pressure, respectively, at position  $\mathbf{x}$  and time  $t$ .  $\Omega$  denotes the entire computational domain, and  $\Gamma_h$  and  $\Gamma_g$  are the portion of the boundary where a Neumann and Dirichlet boundary condition is imposed, respectively.  $N_c$  and  $T$  are the number and duration of cardiac cycles.  $\hat{g}_i(\mathbf{x}, t) \in \mathbb{R}$  and  $\hat{h}(\mathbf{x}, t) \in \mathbb{R}$  are the imposed Dirichlet and Neumann boundary conditions, respectively, and  $n_j$  denotes the normal direction at the Neumann boundaries. Note that the Neumann boundary condition is simplified by decoupling the velocity components, which is common for cardiovascular applications [48, 49, 31].

To write (1) in the frequency domain, we take advantage of the underlying frequency of the flow field,  $\omega = 2\pi/T$ , calculated from the duration of the cardiac cycle. With this knowledge, we can write the solution and boundary conditions in a discretized and truncated frequency form up to the  $M$ -th frequency mode as

$$\begin{aligned}
\hat{u}_i(\mathbf{x}, t) &= \sum_{|m| < M} u_{mi}^*(\mathbf{x}) e^{\hat{i}m\omega t}, \\
\hat{p}(\mathbf{x}, t) &= \sum_{|m| < M} p_m^*(\mathbf{x}) e^{\hat{i}m\omega t}, \\
\hat{g}_i(\mathbf{x}, t) &= \sum_{|m| < M} g_{mi}^*(\mathbf{x}) e^{\hat{i}m\omega t}, \\
\hat{h}(\mathbf{x}, t) &= \sum_{|m| < M} h_m^*(\mathbf{x}) e^{\hat{i}m\omega t},
\end{aligned} \tag{2}$$

where

$$g_{mi}^*(\mathbf{x}) := \frac{1}{T} \int_0^T \hat{g}_i(\mathbf{x}, t) e^{-im\omega t} dt,$$

$$h_m^*(\mathbf{x}) := \frac{1}{T} \int_0^T \hat{h}(\mathbf{x}, t) e^{-im\omega t} dt,$$

are the Fourier coefficients computed such that the spectral content of the boundary conditions is exact up to the  $M$ -th mode. This way, the error associated with discretizing the boundary conditions in (2) scales with the frequency content of the truncated terms and is minimized. The asterisk (\*) denotes the variables in frequency and  $i = \sqrt{-1}$ .

To write the frequency Navier-Stokes equation in a compact matrix form, we organize unknowns and boundary conditions in vectors as

$$\mathbf{u}_i^*(\mathbf{x}) := \begin{bmatrix} u_{(-M+1)i}^* \\ \vdots \\ u_{0i}^* \\ \vdots \\ u_{(M-1)i}^* \end{bmatrix}, \quad \mathbf{p}^*(\mathbf{x}) := \begin{bmatrix} p_{-M+1}^* \\ \vdots \\ p_0^* \\ \vdots \\ p_{M-1}^* \end{bmatrix}, \quad \mathbf{g}_i^*(\mathbf{x}) := \begin{bmatrix} g_{(-M+1)i}^* \\ \vdots \\ g_{0i}^* \\ \vdots \\ g_{(M-1)i}^* \end{bmatrix}, \quad \mathbf{h}^*(\mathbf{x}) := \begin{bmatrix} h_{-M+1}^* \\ \vdots \\ h_0^* \\ \vdots \\ h_{M-1}^* \end{bmatrix}. \quad (3)$$

With these definitions, (1) is expressed in the frequency domain as

$$\begin{aligned} \rho \boldsymbol{\Omega} \mathbf{u}_i^* + \rho \mathbf{A}_j \frac{\partial \mathbf{u}_i^*}{\partial x_j} &= -\frac{\partial \mathbf{p}^*}{\partial x_i} + \frac{\partial}{\partial x_j} \left( \mu \frac{\partial \mathbf{u}_i^*}{\partial x_j} \right), & \text{in } \Omega \\ \frac{\partial \mathbf{u}_i^*}{\partial x_i} &= 0, & \text{in } \Omega \\ \mathbf{u}_i^* &= \mathbf{g}_i^*, & \text{on } \Gamma_g \\ -\mathbf{p}^* n_i + \mu \frac{\partial \mathbf{u}_i^*}{\partial x_j} n_j &= \mathbf{h}^* n_i, & \text{on } \Gamma_h \end{aligned} \quad (4)$$

where the frequency-source matrix,  $\boldsymbol{\Omega}$ , is a diagonal matrix with imaginary entries,  $\boldsymbol{\Omega}(j, j) := \hat{i}(j - M)\omega$ , and  $\mathbf{A}_i$  is a convolution matrix given as  $\mathbf{A}_i(j, k) := u_{(j-k)i}^*$ ,  $|j - k| < M$ . The constraint  $|j - k| < M$  results in zero entries on the top right and bottom left of  $\mathbf{A}_i$ , which eliminates the aliasing effect by preventing the generation of frequency that is equal or higher than  $M$  through the nonlinear convective acceleration term.

In our previous paper, we used the finite element method with a specialized stabilization scheme to solve equations (4) [31]. The computation of the specialized stabilization terms requires  $O(M^2)$  operations, owing to the full convective mode-coupling matrix  $\mathbf{A}$ . As a result, the simulation cost scales quadratically with the number of frequency modes. This second-order scaling diminished the frequency formulation's cost advantage as the number of frequencies captured in a simulation increased.

In order to achieve first-order cost scaling, we use a transformation of the frequency Navier-Stokes equations proposed in a previous harmonic balance method paper [47]. We write the vectors containing the variables in frequency as discrete Fourier operations

$$\mathbf{u}_i^*(\mathbf{x}) := \mathbf{E} \mathbf{u}_i(\mathbf{x}), \quad \mathbf{p}^*(\mathbf{x}) := \mathbf{E} \mathbf{p}(\mathbf{x}), \quad \mathbf{g}_i^*(\mathbf{x}) := \mathbf{E} \mathbf{g}_i(\mathbf{x}), \quad \mathbf{h}^*(\mathbf{x}) := \mathbf{E} \mathbf{h}(\mathbf{x}), \quad (5)$$

where  $\mathbf{E}$  is the discrete Fourier transform matrix defined as  $\mathbf{E}(j, k) := (1/N) e^{-2\pi i j k / N}$ , where  $j, k = 0, \dots, N - 1$  and  $N = 2M - 1$ . The unknowns and boundary conditions are transformed to vectors that contain variables at  $N$  equally spaced time points in a cycle, given as

$$\mathbf{u}_i(\mathbf{x}) := \begin{bmatrix} u_{0i} \\ u_{1i} \\ \vdots \\ u_{(N-1)i} \end{bmatrix}, \quad \mathbf{p}(\mathbf{x}) := \begin{bmatrix} p_0 \\ p_1 \\ \vdots \\ p_{(N-1)} \end{bmatrix}, \quad \mathbf{g}_i(\mathbf{x}) := \begin{bmatrix} g_{0i} \\ g_{1i} \\ \vdots \\ g_{(N-1)i} \end{bmatrix}, \quad \mathbf{h}(\mathbf{x}) := \begin{bmatrix} h_0 \\ h_1 \\ \vdots \\ h_{(N-1)} \end{bmatrix}. \quad (6)$$

Plugging equations (5) in (4) and multiplying all equations by the discrete inverse Fourier transform matrix,  $\mathbf{E}^{-1}$ , gives us the final form of the harmonic balance Navier-Stokes equation as

$$\begin{aligned}
\rho \mathbf{H} \mathbf{u}_i + \rho \mathbf{U}_j \frac{\partial \mathbf{u}_i}{\partial x_j} &= -\frac{\partial \mathbf{p}}{\partial x_i} + \frac{\partial}{\partial x_j} \left( \mu \frac{\partial \mathbf{u}_i}{\partial x_j} \right), & \text{in } \Omega \\
\frac{\partial \mathbf{u}_i}{\partial x_i} &= 0, & \text{in } \Omega \\
\mathbf{u}_i &= \mathbf{g}_i, & \text{on } \Gamma_g \\
-\mathbf{p} n_i + \mu \frac{\partial \mathbf{u}_i}{\partial x_j} n_j &= \mathbf{h} n_i, & \text{on } \Gamma_h
\end{aligned} \tag{7}$$

where  $\mathbf{H}$  is a zero diagonal time point-coupling matrix where  $\mathbf{H} = \mathbf{E}^{-1} \mathbf{\Omega} \mathbf{E}$ , and  $\mathbf{U}_i$  is a diagonal convective acceleration matrix where  $\mathbf{U}_i = \text{diag}(\mathbf{u}_i)$ .

### Remarks:

1. The harmonic balance equations in (7) is a direct transformation of the frequency equations in (4), using a discrete inverse Fourier transform operator. The solutions retain spectral accuracy as a result of the truncated frequency series used to represent the unknowns.
2. The discretization of the acceleration term arises from expressing the solution and boundary conditions in a truncated frequency form. This approach assumes the solution consists solely of integer multiples of a fundamental frequency,  $\omega$ . This assumption is reasonable for cardiovascular flows because the energy in each mode is either directly injected by the boundary condition or produced through interaction between modes. However, in some instances, another distinct frequency,  $\omega_g$ , may arise from geometry-induced instabilities or turbulence, which is not integer multiples of  $\omega$ . This typically occurs when the Reynolds number in the fluid domain reaches or exceeds the transient flow limit, typically between 2,000 and 3,000. In these cases, the solutions will fail to converge to steady values.
3. Apart from the time-coupling term,  $\rho \mathbf{H} \mathbf{u}_i$ , in equations (7), all other terms can be calculated at each time point independently of other time points. This allows for the existing code structure used to solve conventional time-domain Navier-Stokes equations to remain largely unchanged. Additionally, since  $\mathbf{H}$  is formulated with two discrete Fourier transform matrices, a fast Fourier transform routine can be employed, resulting in a cost scaling of  $O(N \log(N))$ . The implementation details will be discussed in the following sections.

## 2.2 Stabilized finite element method

The discrete finite element form of the Navier Stokes equation, namely the Galerkin form, needs to be stabilized to mitigate nonphysical solution oscillation resulting from discretizing the convective-acceleration and dissipative terms [50, 51, 52]. In addition, a pressure stabilization term is required to allow the use of equal order shape functions [53, 54]. There have been decades of work that proposed various stabilization methods and formulations for the finite element method [55, 56, 57, 58]. In this study, we chose Galerkin/least-squares stabilization (GLS), which produces both of these terms and is consistent with the conventional time formulation used for comparison.

The GLS method for the harmonic balance Navier-Stokes equations is stated as finding  $\mathbf{u}_i^h$  and  $\mathbf{p}^h$  such that for any test functions  $\mathbf{w}_i^h$  and  $\mathbf{q}^h$ , we have

$$\begin{aligned}
& \overbrace{\left( \mathbf{w}_i^h, \rho \mathbf{H} \mathbf{u}_i^h + \rho \mathbf{U}_j \frac{\partial \mathbf{u}_i^h}{\partial x_j} \right)_{\Omega} + \left( \frac{\partial \mathbf{w}_i^h}{\partial x_j}, -\mathbf{p}^h \delta_{ij} + \mu \frac{\partial \mathbf{u}_i^h}{\partial x_j} \right)_{\Omega} + \left( \mathbf{q}^h, \frac{\partial \mathbf{u}_i^h}{\partial x_i} \right)_{\Omega}}^{\text{Galerkin's terms}} \\
& + \underbrace{\left( \mathcal{L}_i(\mathbf{w}_i^h, \mathbf{q}^h), \frac{\tau}{\rho} \mathcal{L}_i(\mathbf{u}_i^h, \mathbf{p}^h) \right)_{\tilde{\Omega}}}_{\text{Least-square stabilization terms}} = \underbrace{\left( \mathbf{w}_i^h, \mathbf{h} n_i \right)_{\Gamma_h}}_{\text{Neumann BCs. terms}}, \tag{8}
\end{aligned}$$

where

$$\mathcal{L}_i(\mathbf{u}_i^h, \mathbf{p}^h) := \rho \mathbf{H} \mathbf{u}_i^h + \rho \mathbf{U}_j \frac{\partial \mathbf{u}_i^h}{\partial x_j} + \frac{\partial \mathbf{p}^h}{\partial x_i} - \frac{\partial}{\partial x_j} \left( \mu \frac{\partial \mathbf{u}_i^h}{\partial x_j} \right),$$

is the momentum equation differential operator. The inner product notation for two vector functions  $\mathbf{f}(\mathbf{x})$  and  $\mathbf{g}(\mathbf{x})$  over  $S$  is defined as

$$\left( \mathbf{f}, \mathbf{g} \right)_S := \int_S \mathbf{f}^\top \mathbf{g} dS. \quad (9)$$

$\tilde{\Omega}$  on the stabilization terms indicates elemental integration. Note that the terms corresponding to the Dirichlet boundary conditions are not included in (8) as  $\mathbf{u}_i^h = \mathbf{g}_i$  and  $\mathbf{w}_i^h = \mathbf{0}$  on  $\Gamma_g$  are directly built into the solution and trial functions spaces, respectively.

The stabilization parameter  $\boldsymbol{\tau}$  in (8) plays a vital role in the performance of the stabilization method. It is defined such that in the steady limit when  $\omega = 0$ , the equations recover the traditional GLS stabilization parameter as in the conventional finite element formulations [59, 60]. Since the convective matrix  $\mathbf{U}_j$  is diagonal,  $\boldsymbol{\tau}$  becomes a diagonal matrix,  $\boldsymbol{\tau} = \text{diag}(\tau_0, \tau_1, \dots, \tau_{(N-1)})$ , which entries can be calculated pointwise for each time point as

$$\tau_n = \left( u_{ni}^h \cdot \boldsymbol{\xi} u_{ni}^h + C_1 \nu^2 \boldsymbol{\xi} : \boldsymbol{\xi} \right)^{-\frac{1}{2}}, n \in [0, N) \quad (10)$$

where  $\nu$  is the kinematic viscosity,  $\boldsymbol{\xi}$  is the covariant tensor obtained from the mapping of the physical-parent elements, and  $C_1$  is a shape-function-dependent constant, which is 3 in our study.

#### Remarks:

1. The least-square stabilization terms encapsulate two traditional stabilization terms, the streamline upwind Petrov/Galerkin (SUPG) term  $\rho \mathbf{U}_j \frac{\partial \mathbf{w}_i^h}{\partial x_j} \boldsymbol{\tau} \mathbf{U}_k \frac{\partial \mathbf{u}_i^h}{\partial x_k}$ , and the pressure stabilized Petrov/Galerkin (PSPG) term  $\frac{1}{\rho} \frac{\partial \mathbf{q}^h}{\partial x_i} \boldsymbol{\tau} \frac{\partial \mathbf{p}^h}{\partial x_i}$ . However, relying solely on the SUPG/PSPG terms will lead to solution instabilities. Including the full differential operator  $\mathcal{L}$ , which contains the  $\mathbf{H}$  terms, is essential for ensuring the stability of this method. This approach contrasts with the stabilization for traditional time-stepping solvers, where the acceleration contribution in  $\mathcal{L}$  is often neglected.
2. Expanding the least-square stabilization terms reveals that this stabilization method resembles the residual-based variational multiscale method (RBVMS) [61, 62, 33], where the subscale velocity  $\mathbf{u}'_i$  is included only on the time-coupling term and the velocity gradient in the convection term, i.e.

$$\left( \mathbf{w}_i^h, \rho \mathbf{H} (\mathbf{u}_i^h + \mathbf{u}'_i) + \rho \mathbf{U}_j \frac{\partial (\mathbf{u}_i^h + \mathbf{u}'_i)}{\partial x_j} \right)_\Omega.$$

Note that the diffusive term is dropped from  $\mathcal{L}$  because we use linear interpolation functions. We also tested incorporating the full RBVMS terms, similar to the stabilization method in [61], by adding  $\mathbf{u}'_i$  to all velocity terms. We observed that the RBVMS formulation is less stable than the GLS method, particularly near the transition flow regime. However, the solution convergence rate achieved with RBVMS is slightly faster than that with GLS.

3. The GLS method yields accurate results when the flow Womersley number is small, which is valid in cardiovascular simulations where the cardiac cycle frequency is small and the mesh resolution is high. We have previously introduced a specialized stabilization method that yields superior accuracy [30].
4. The conventional design of the stabilization parameter  $\boldsymbol{\tau}$  for unsteady problems includes a time-discretization or frequency term proportional to  $\Delta t$  or  $1/\omega$ , respectively [63]. This term helps stabilize the solution in highly unsteady flows. However, in our cases, we have not observed any difference in convergence or the final solution with the inclusion of this term. This is due to the low element Womersley numbers in our cardiovascular simulations, defined as  $\beta := h \sqrt{\frac{(N-1)\omega}{2\nu}}$ . When  $\beta < 1$ , the contribution of the frequency term to  $\boldsymbol{\tau}$  becomes negligible. In all the cases examined in this study, we found that  $\beta < 0.2$ .

## 2.3 Solution Procedure

This section provides an overview of the solution procedure used to solve equation (8). We assume all interpolation functions are linear in the following derivations, consistent with what is commonly used in finite element solvers specialized for cardiovascular flow. As a result, we drop the second derivative terms that cannot be transformed into first derivatives through integration by parts. The unknowns for all time points are solved simultaneously, resulting in  $4N$  unknowns on each interior node. The Newton-Raphson method is employed for iterative root-finding. Additionally, we apply matrix splitting to the tangent matrix, enabling the use of fast Fourier transforms during matrix-vector multiplications. A pseudo time-stepping scheme, developed in our previous study, is utilized here to improve the convergence of the solver [31].

The test functions  $\mathbf{w}_i^h$  and  $\mathbf{q}^h$  in (8) are discretized in space using

$$\begin{aligned}\mathbf{w}_i^h(\mathbf{x}) &= \sum_A \mathbf{c}_{Ai}^w N_A(\mathbf{x}), \\ \mathbf{q}^h(\mathbf{x}) &= \sum_A \mathbf{c}_A^q N_A(\mathbf{x}),\end{aligned}$$

where  $N_A(\mathbf{x})$  is the interpolation function associated with node  $A$ . Since  $\mathbf{w}_i^h$  and  $\mathbf{q}^h$  are arbitrary functions, (8) must hold for any  $\mathbf{c}_{Ai}^w$  and  $\mathbf{c}_A^q$ . That permits us to obtain a system of equations from (8), which are

$$\begin{aligned}\mathbf{r}_{Ai}^m &= \int_{\Omega} \left( \rho N_A \mathbf{H} \mathbf{u}_i^h + \rho N_A \mathbf{U}_j \frac{\partial \mathbf{u}_i^h}{\partial x_j} - \frac{\partial N_A}{\partial x_i} \mathbf{p}^h + \mu \frac{\partial N_A}{\partial x_j} \frac{\partial \mathbf{u}_i^h}{\partial x_j} \right) d\Omega - \int_{\Gamma_h} N_A \mathbf{h} n_i d\Gamma \\ &\quad + \int_{\tilde{\Omega}} \left( -\mathbf{H} N_A + \mathbf{U}_j \frac{\partial N_A}{\partial x_j} \right) \boldsymbol{\tau} \mathcal{L}_i(\mathbf{u}_i^h, \mathbf{p}^h) d\Omega = \mathbf{0}, \quad A \in \eta - \eta_g, \quad i = 1, 2, \text{ and } 3, \\ \mathbf{r}_A^c &= \int_{\Omega} N_A \frac{\partial \mathbf{u}_i^h}{\partial x_i} d\Omega + \int_{\tilde{\Omega}} \frac{1}{\rho} \frac{\partial N_A}{\partial x_i} \boldsymbol{\tau} \mathcal{L}_i(\mathbf{u}_i^h, \mathbf{p}^h) d\Omega = \mathbf{0}, \quad A \in \eta.\end{aligned}\tag{11}$$

In (11),  $\eta$  and  $\eta_g$  denote the set of nodes in the entire domain  $\Omega$  and those located on the Dirichlet boundaries  $\Gamma_g$ , respectively. It is important to note that the negative sign in front of the  $\mathbf{H} N_A$  in the least-square term arises from taking the transpose on the left differential operator. Since  $\mathbf{H}$  is a skew-symmetric matrix and  $\mathbf{U}_j$  is a diagonal matrix, we can write the transpose as  $\mathbf{H}^\top = -\mathbf{H}$  and  $\mathbf{U}_j^\top = \mathbf{U}_j$ .

The velocity and pressure are discretized using the same interpolation functions as those of the test functions, namely

$$\begin{aligned}\mathbf{u}_i^h(\mathbf{x}) &= \sum_A \mathbf{u}_{Ai}^d N_A(\mathbf{x}), \\ \mathbf{p}^h(\mathbf{x}) &= \sum_A \mathbf{p}_A^d N_A(\mathbf{x}),\end{aligned}$$

where  $\mathbf{u}_{Ai}^d$  and  $\mathbf{p}_A^d$  contain velocity and pressure, respectively, at all time points at node  $A$ . In our implementation, we build the Dirichlet boundary condition into the unknown vector so that  $\mathbf{u}_{Ai}^d = \mathbf{g}_i(\mathbf{x}_A)$ , where  $\mathbf{x}_A$  is the position of node  $A$ .

At the discrete level, our goal is to find  $\mathbf{u}_{Ai}^d$  and  $\mathbf{p}_A^d$  such that all equations in (11) are satisfied. Given that these equations are nonlinear, we accomplish this through an iterative process using the Newton-Raphson iterations, given as solving

$$\mathbf{y}^{(n+1)} = \mathbf{y}^{(n)} - \left( \mathbf{L}^{(n)} \right)^{-1} \mathbf{r}^{(n)}\tag{12}$$

at each Newton-Raphson iteration  $n$  to update the solution from the last iteration  $\mathbf{y}^{(n)}$  and compute it at the next iteration  $\mathbf{y}^{(n+1)}$ .  $\mathbf{r}^{(n)}$  is the residual vector calculated based on the unknowns at the previous iteration  $n$  using (11) and  $\mathbf{L}^{(n)}$  is the tangent matrix calculated from  $\mathbf{y}^{(n)}$ . The unknowns and residuals are written in vectors as

$$\mathbf{y} := \begin{bmatrix} \mathbf{u}_1^d \\ \mathbf{u}_2^d \\ \mathbf{u}_3^d \\ \mathbf{p}^d \end{bmatrix}, \quad \mathbf{r} := \begin{bmatrix} \mathbf{r}_1^m \\ \mathbf{r}_2^m \\ \mathbf{r}_3^m \\ \mathbf{r}^c \end{bmatrix},$$

Before presenting the form of the tangent matrix, it is clear that all terms not containing the matrix  $\mathbf{H}$  in (11) can be calculated pointwise. This means that the residual at each time point can be calculated using only the unknowns associated with that specific time point, provided that the terms involving the time-coupling acceleration matrix  $\mathbf{H}$  can be calculated separately. With this understanding, we perform matrix splitting on the tangent matrix  $\mathbf{L}^{(n)}$  to separate time-coupling terms from the non-coupled terms as

$$\mathbf{L} = \frac{\partial \mathbf{r}}{\partial \mathbf{y}} = \mathbf{C} + \mathbf{P}, \quad (13)$$

where the superscript  $(n)$  is dropped to simplify the notation. The form of the tangent matrix  $\mathbf{P}$  is essentially identical to that of a conventional steady-state finite element Navier-Stokes solver as,

$$\mathbf{P} = \begin{bmatrix} \mathbf{K} & \mathbf{0} & \mathbf{0} & \mathbf{G}_1 \\ \mathbf{0} & \mathbf{K} & \mathbf{0} & \mathbf{G}_2 \\ \mathbf{0} & \mathbf{0} & \mathbf{K} & \mathbf{G}_3 \\ \mathbf{D}_1 & \mathbf{D}_2 & \mathbf{D}_3 & \mathbf{L} \end{bmatrix}, \quad (14)$$

where

$$\begin{aligned} \mathbf{K}_{AB} &= \int_{\Omega} \left( \rho N_A \mathbf{U}_k \frac{\partial N_B}{\partial x_k} + \mu \frac{\partial N_A}{\partial x_k} \frac{\partial N_B}{\partial x_k} \mathbf{I} \right) d\Omega + \int_{\tilde{\Omega}} \mathbf{U}_k \frac{\partial N_A}{\partial x_k} \rho \boldsymbol{\tau} \mathbf{U}_k \frac{\partial N_B}{\partial x_k} d\Omega, \\ (\mathbf{G}_{AB})_i &= - \int_{\Omega} \frac{\partial N_A}{\partial x_i} N_B \mathbf{I} d\Omega + \int_{\tilde{\Omega}} \mathbf{U}_k \frac{\partial N_A}{\partial x_k} \boldsymbol{\tau} \frac{\partial N_B}{\partial x_i} d\Omega, \\ (\mathbf{D}_{AB})_j &= \int_{\Omega} N_A \frac{\partial N_B}{\partial x_j} \mathbf{I} d\Omega + \int_{\tilde{\Omega}} \frac{\partial N_A}{\partial x_j} \boldsymbol{\tau} \mathbf{U}_k \frac{\partial N_B}{\partial x_k} d\Omega, \\ \mathbf{L}_{AB} &= \int_{\tilde{\Omega}} \frac{1}{\rho} \frac{\partial N_A}{\partial x_k} \boldsymbol{\tau} \frac{\partial N_B}{\partial x_k} d\Omega. \end{aligned} \quad (15)$$

It is important to note that all blocks in matrix  $\mathbf{P}$  are diagonal matrices. Therefore, the computational cost associated with matrix multiplications of  $\mathbf{P}$  is  $O(N)$  using a sparse matrix implementation.

The time point-coupling tangent matrix  $\mathbf{C}$  handles all terms involving the  $\mathbf{H}$  matrix. It includes one contribution from the Galerkin's terms and four contributions from the least-squares stabilization terms in (7). Our numerical experiments showed that dropping the stabilization terms' contribution to  $\mathbf{C}$  has a negligible effect on solution convergence. Therefore, we neglect the tangent contributions from these terms, which simplifies the number of operations needed to compute  $\mathbf{C}$ . It is important to note that this simplification applies only to the calculation of the tangent matrix and not to the residual, ensuring no impact on the final converged solution. The simplified time-coupling tangent matrix takes the following form

$$\mathbf{C} = \begin{bmatrix} \mathbf{F} & \mathbf{0} & \mathbf{0} & \mathbf{0} \\ \mathbf{0} & \mathbf{F} & \mathbf{0} & \mathbf{0} \\ \mathbf{0} & \mathbf{0} & \mathbf{F} & \mathbf{0} \\ \mathbf{0} & \mathbf{0} & \mathbf{0} & \mathbf{0} \end{bmatrix}, \quad (16)$$

where

$$\mathbf{F}_{AB} = \mathbf{H} \int_{\Omega} \rho N_A \mathbf{I} N_B d\Omega, \quad (17)$$

The matrix  $\mathbf{H}$  is formulated as  $\mathbf{H} = \mathbf{E}^{-1} \boldsymbol{\Omega} \mathbf{E}$ . The matrix multiplications involving  $\mathbf{E}$  and  $\mathbf{E}^{-1}$  can be efficiently handled using a fast Fourier transform (FFT) and an inverse fast Fourier transform (IFFT), respectively. This implementation reduces the computational cost of performing matrix-vector multiplications involving  $\mathbf{H}$  from  $O(N^2)$  to  $O(N \log(N))$ . When combined with the cost of computing other terms, the overall cost-scaling for the solver becomes approximately  $O(N)$ . This study used the open-source library FFTW [64] to execute the fast Fourier transforms.

Before solving the final linear system, a pseudo time-stepping scheme is added to improve linear solver convergence and reduce the overall cost. Pseudo time-stepping schemes have been used previously in solving



harmonic balance equations [47] and the specific method used here was proposed in our previous study [31]. The implementation of the pseudo time-stepping involves adding

$$\left( \mathbf{w}_i^h, \rho \frac{\partial \mathbf{u}_i^h}{\partial \tilde{t}} \right)_{\Omega}, \quad (18)$$

to (8), and integrating  $\mathbf{u}_i^h$  in pseudo-time  $\tilde{t}$  similar to the conventional time formulation of the Navier-Stokes equation. Using the generalized- $\alpha$  method [65], the tangent matrix is supplemented by adding

$$\left( N_A, \frac{c_1 \rho}{\Delta \tilde{t}} N_B \mathbf{I} \right)_{\Omega}, \quad (19)$$

to  $\mathbf{K}_{AB}$  in (15), where we used  $\rho_{\infty} = 0$  resulting in  $c_1 = 1.5$ . Since the pseudo time step term goes to zero as the solution converges to a steady result, it improves the convergence behavior without affecting the final solution.

The choice of the pseudo time step size  $\Delta \tilde{t}$  is essential for achieving optimal convergence. Our numerical experiments show that the system of equations will generally converge when the convective Courant–Friedrichs–Lewy (CFL) number calculated from the pseudo time step size is  $O(1)$  or less, defined as

$$C_{\text{CFL}} = \frac{u_c \Delta \tilde{t}}{h_c}, \quad (20)$$

where the characteristic length,  $h_c$ , is taken as the mean element edge length of the domain and the characteristic convective velocity,  $u_c$ , is taken as the mean velocity at the inlet boundary at the maximum flow rate for the inlet flow profile. Therefore, the optimal choice of pseudo time step size can be approximated as

$$\Delta \tilde{t} \sim \frac{h_c}{u_c}.$$

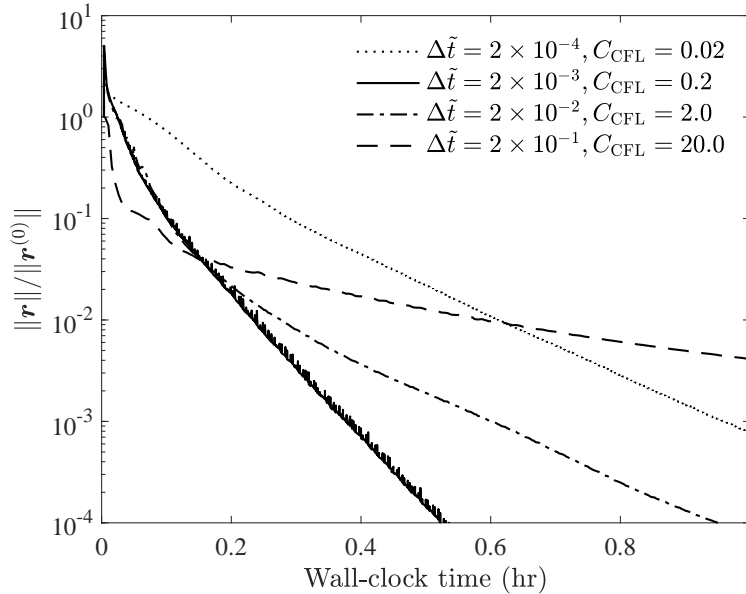


Figure 1: Simulation convergence speed for four pseudo time step sizes,  $\Delta \tilde{t}$ . The y-axis is the relative residual compared to the residual at the initialization step,  $\|\mathbf{r}\|/\|\mathbf{r}^{(0)}\|$ .

To illustrate the impact of the CFL number on convergence, we conducted four identical simulations, varying only the pseudo time step size. These simulations are based on the  $N = 13$  case in Section 3.2. As shown in Figure 1, the simulation with a large CFL number converges exceptionally slowly. Conversely, an excessively small CFL number also unnecessarily increases simulation costs due to the cost of constructing

the linear system at each step. It is important to note that optimal CFL number and pseudo time step size for achieving the fastest convergence may vary depending on other factors, such as the geometry of the case, mesh uniformity, and flow dynamics. Generally, optimal convergence is attained when the CFL number is around 1.

A backflow stabilization scheme is used to prevent numerical instabilities caused by reversal flow through  $\Gamma_h$ , where a Neumann boundary condition is imposed. This method is identical to the backflow stabilization scheme used in conventional time-stepping Navier-Stokes finite element solver [66]. The stabilization is achieved by adding

$$\left( \mathbf{w}_i^h, \frac{\rho}{2} \beta |\mathbf{U}_i n_i|_- \mathbf{u}_i^h \right)_{\Gamma_h}, \quad (21)$$

to the right-hand side of (8), where

$$|\mathbf{U}_i n_i|_- = \frac{\mathbf{U}_i n_i - |\mathbf{U}_i n_i|}{2},$$

and  $\beta \in [0, 1]$  is a user-defined coefficient, which we used  $\beta = 0.2$  in all cases.

We applied a standard Jacobi preconditioner on the tangent matrix  $\mathbf{L}$  to improve the conditioning of the linear system [67]. Since  $\mathbf{C}$  is a zero diagonal matrix, the preconditioner only consists of the diagonal entries of matrix  $\mathbf{P}$ . To solve the linear system, we utilized the generalized minimal residual method (GMRES) [68]. Simulations are considered converged once the two-norm of the residual decreases by three orders of magnitude, as established in our previous study [31].

### 3 Results

The proposed harmonic balance solver is constructed from our in-house finite-element solver named Multiphysics finite-element solver (MUPFES) [3, 69]. The solver has been verified [70] and extensively employed for cardiovascular modeling in the past [12, 71, 16]. This solver is parallelized using a message passing interface (MPI) and a specialized parallelization strategy [72, 73]. The workload is parallelized using spatial partitioning by employing ParMETIS library [74]. All computations are performed on a cluster of AMD Opteron™ 6378 processors that are interconnected via a QDR Infiniband.

In this section, we primarily focus on comparing the accuracy and cost of the proposed harmonic balance CFD solver with the conventional time-stepping CFD solver. To ensure consistency, the time-stepping CFD solver also utilizes the GLS stabilization method. However, unlike the proposed solver, the stabilization parameter for the time solver,  $\hat{\tau}$ , includes a contribution from the acceleration term to improve numerical stability. The exact form was introduced in a prior paper as [63]

$$\hat{\tau} = (\hat{\omega}^2 + \hat{u}_i^h \cdot \boldsymbol{\xi} \hat{u}_i^h + C_1 \nu^2 \boldsymbol{\xi} : \boldsymbol{\xi})^{-\frac{1}{2}}, \quad (22)$$

where  $\hat{\omega} = \|\frac{\partial \hat{u}_i^h}{\partial t}\|_{\Omega} / \|\hat{u}_i^h\|_{\Omega}$ . The code structure of the time-stepping and harmonic balance solvers are kept as identical as possible for comparison purposes. The linear solver (GMRES) tolerance is set at 0.03 for both solvers. The time solver Newton-Raphson iteration tolerance is set at three order of magnitudes, consistent with the convergence criteria of the harmonic balance solver. We conducted simulations on three cardiovascular cases using both solvers: a Glenn procedure case involving pulmonary arteries, a cerebral artery case, and a left main coronary artery case. These cases were chosen to represent a wide range of scenarios, distinguished both numerically and hemodynamically. The geometries and inlet flow rate for these cases were obtained from an online repository [75]. The Reynolds number for the Glenn case is higher than that of the other two, featuring a smooth inflow profile that can be accurately captured with just a few time points. In contrast, the cerebral arteries case presents a more complex smooth inflow profile with higher geometric complexity. Meanwhile, the left main coronary artery case has distinct kinks in the inflow profile, which requires a significant number of time points to represent accurately.

The outlets in this study are modeled as Neumann boundaries with fixed physiological pressure values. Previous cardiovascular simulations have treated the outlets as resistance boundaries to achieve more realistic outlet responses [12, 76]. However, implementing the resistance boundary for the harmonic balance solver is beyond the scope of this study. All walls are assumed to be non-moving and non-slip. The whole blood density ( $\rho = 1.06 \text{ g/cm}^3$ ) and dynamic viscosity ( $\mu = 4 \text{ mPa} \cdot \text{s}$ ) are constant across all cases. These results

aim to demonstrate the solution validity and cost efficiency of the harmonic balance solver as an alternative to the conventional time-stepping solver. Since the geometries and boundary conditions in all cases are physiological, we will also briefly discuss the clinical relevance of each case.

### 3.1 Glenn pulmonary flow

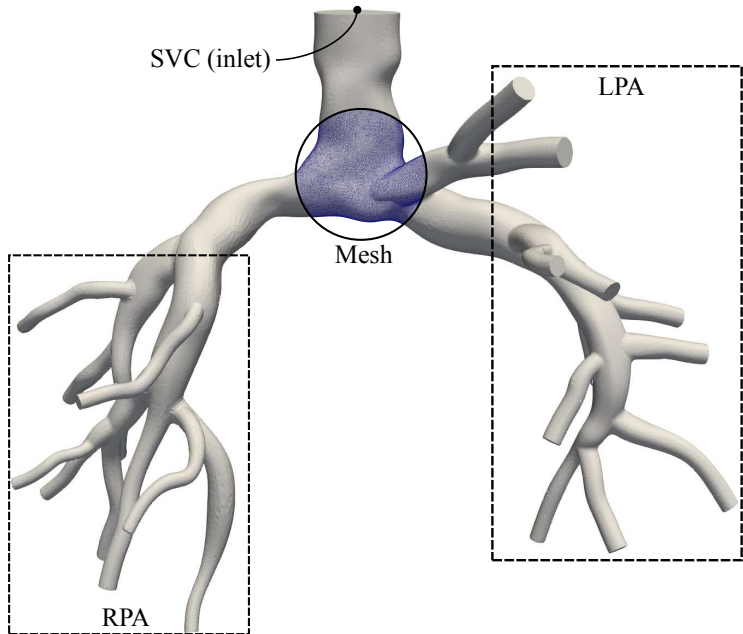


Figure 2: Clinically obtained Glenn pulmonary geometry with a sectional view of the mesh. SVC, superior vena cava; LPA, left pulmonary artery; RPA, right pulmonary artery.

The Glenn procedure is an early-stage surgical intervention designed for patients with single ventricle birth defects [77, 78]. The operation establishes the pulmonary circulation by directly connecting the superior vena cava (SVC) to the pulmonary arteries (PA), as shown in the geometry in Figure 2. Prior studies have utilized this geometry to conduct conventional CFD simulations [76]. The inflow boundary condition is taken from the prior study, providing the SVC flow rate as a function of time during a cardiac cycle. The outlet boundaries are set at a steady pressure of 7.5 mmHg. The cardiac cycle duration is 0.6979 seconds, and the peak Reynolds number is around 1,000.

In total, four simulations are performed: one using the conventional time-stepping CFD solver and ran for four cardiac cycles (4,000 time steps), and three using the harmonic balance solver with varying numbers of time points ( $N = 7, 13, \text{ and } 19$ ). The geometry is discretized with 1,946,676 tetrahedral elements. For the harmonic balance simulations, the pseudo time step size is  $\Delta\tilde{t} = 5 \times 10^{-3}$  resulting in  $C_{CFL} = 2.5$ . The inlet boundary conditions for the harmonic balance simulations are generated by performing a Fourier transform on the inflow profile, followed by a discrete inverse Fourier transform on the truncated Fourier series, as defined in Equations (2) and (5). The resulting inlet boundary conditions are depicted in Figure 3. As shown in the boundary condition plots, this inlet profile for this case is smooth and can be accurately captured with a few time points. The truncation error for the inflow profile is already less than 1% for  $N = 13$ .

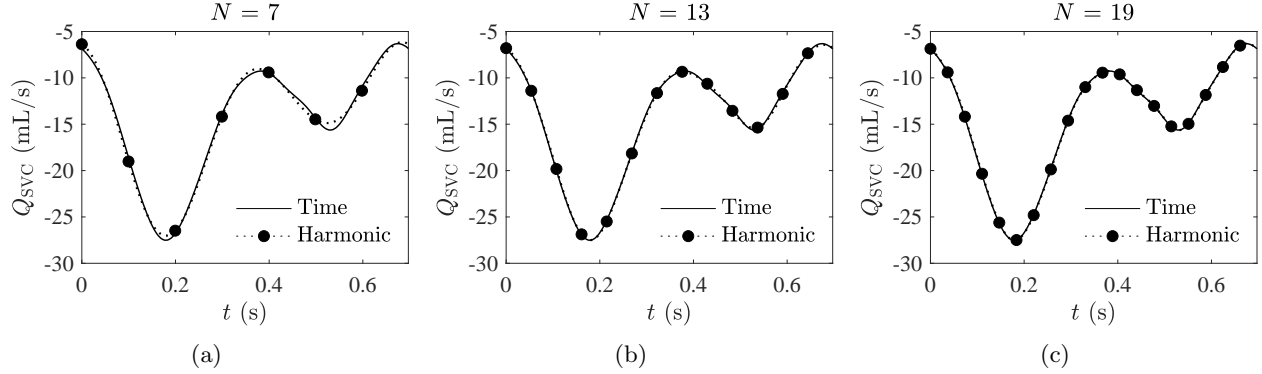


Figure 3: Discretized harmonic balance boundary conditions at each time point (black circle) on the SVC inlet. The dotted line represents the reconstructed profile from the time points. For reference, the solid line is the original flow profile in time. (a)  $N = 7$ , (b)  $N = 13$ , (c)  $N = 19$ .

All simulations were conducted on our in-house cluster using 288 cores operating at 2.4 GHz. Figure 4 illustrates the cost of performing the harmonic balance simulations. The left axis shows the wall-clock time of the simulations, and the right axis indicates the speedup compared to the conventional time-stepping simulation. The conventional simulation took 50 wall-clock hours to complete. The figure is presented on a log-log scale to highlight the linear cost scaling of our solver as the number of time points increases. The harmonic balance simulation using  $N = 3$  was included solely to demonstrate cost scaling. For the case with the largest number of time points  $N = 19$  the harmonic balance simulation is still 40 times faster than the conventional simulation.

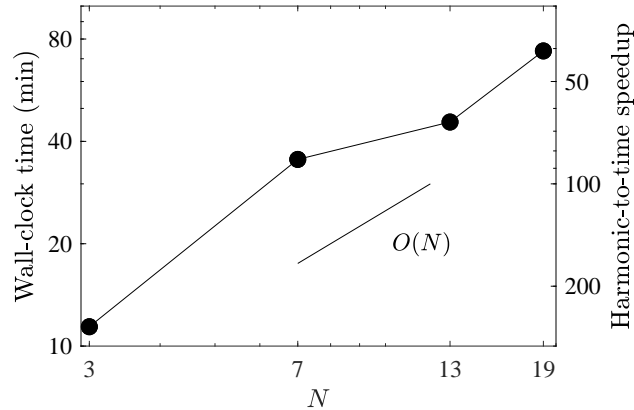


Figure 4: The cost and speed-up of the harmonic balance solver for the pulmonary flow case. The left axis shows the wall-clock time of the harmonic balance simulations. The right axis shows the speedup of the harmonic balance simulations compared to the conventional time-stepping simulation. A linear scaling line is included for reference.

To obtain the continuous temporal solution of the flow field, we can perform a Fourier transform on the time-point solutions. We then reconstruct the temporal solution from the obtained Fourier modes, as defined in Equation 2. Figure 5 illustrates the velocity and pressure fields at  $t = 0.2s$  of the cardiac cycle, when the inlet flow rate reaches its peak. Qualitative differences are only observed in the  $N = 7$  case at certain locations in the domain, such as the SVC-PA junction.

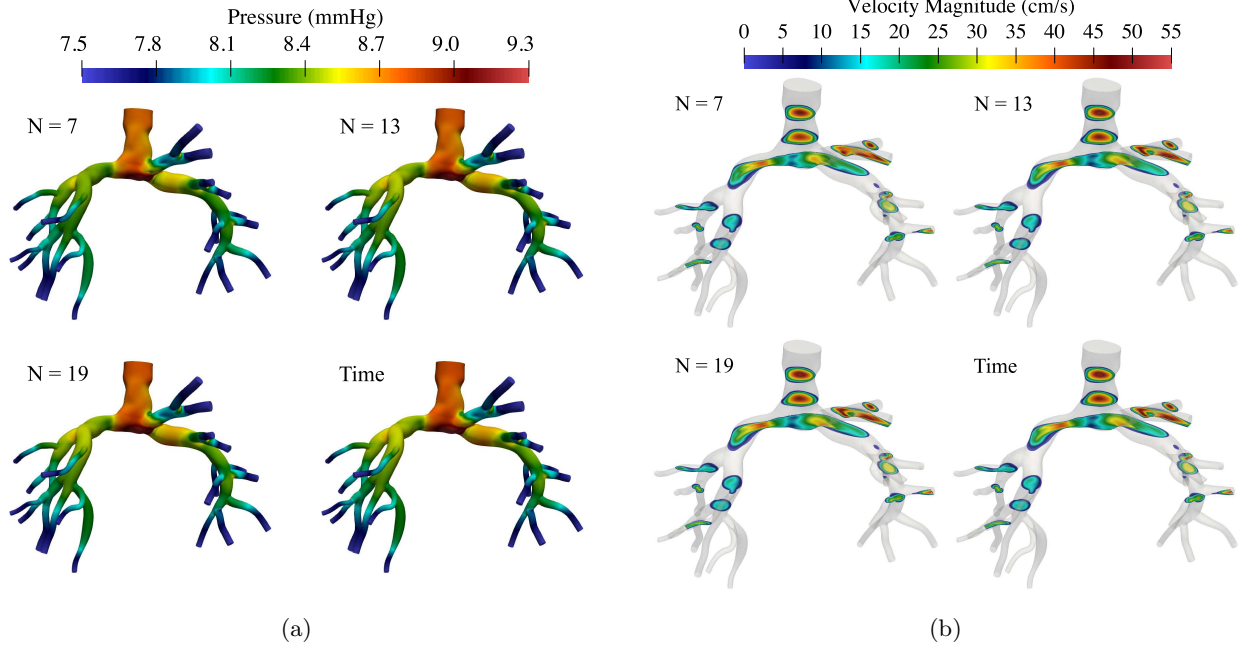


Figure 5: Harmonic balance results using  $N = 7, 13,$  and  $19$  compared to the conventional time results for the pulmonary flow case. The (a) pressure and (b) velocity magnitude contours are taken at  $t = 0.2$  seconds of the cardiac cycle.

In addition to qualitatively examining the velocity and pressure fields, we aim to establish a quantitative measurement for the relative accuracy of the harmonic balance solver compared to the conventional time solver. To achieve this, we introduce a notation for the integrated relative root mean squared error,  $E_X^{f(x)}$ , as a measure of result error. The error is defined as

$$E_X^{f(x)} = \frac{\int_X \|f_{\text{harmonic}}(x) - f_{\text{time}}(x)\| dx}{\int_X \|f_{\text{time}}(x)\| dx}, \quad (23)$$

where the dependent variable  $f(x)$  can represent either the velocity vector,  $\mathbf{u}$ , or the pressure,  $p$ . The subscripts indicate whether the results are taken from the harmonic balance solver or the conventional time solver. The integral can be performed over the geometry,  $\Omega$ , the cardiac cycle,  $T$ , or both.

Using this definition, we can calculate the spacial integral relative error for both velocity and pressure, and then plot these errors over one cardiac cycle, as shown in Figure 6. Note that the curves appear unsmooth because we recorded the results from the conventional time solver every 50 time steps for processing, resulting in 20 data points for the error calculation.

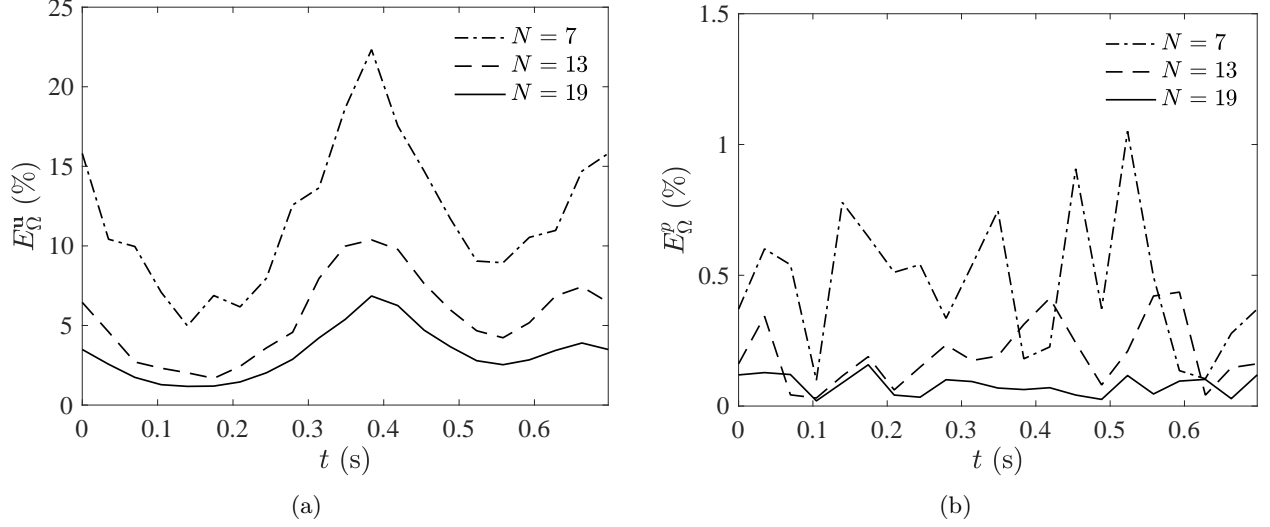


Figure 6: The volumetric integral relative root mean square error over the fluid domain for (a) the velocity vector and (b) the pressure as functions of time in the cardiac cycle of the pulmonary flow.

We can further analyze the error by integrating it over one cycle and observe the trend as the harmonic balance time point resolution ( $N$ ) increases. As depicted in Figure 7a, the error of the variables is integrated both across the fluid domain,  $\Omega$ , and over one cardiac cycle,  $T$ . The pressure relative error is considerably smaller than the velocity error because the Neumann outlets are set at a fixed value that is much larger than the range of pressure in the solution. The velocity error decreases substantially as the number of time points increases, falling to less than 5% when  $N = 19$ . This result also demonstrates that while the inlet flow profile can be well represented with  $N = 7$ , due to the intermediate Reynolds number of this case ( $Re = 1000$ ), more than seven time points are required to accurately capture the dynamics of the fluid field.

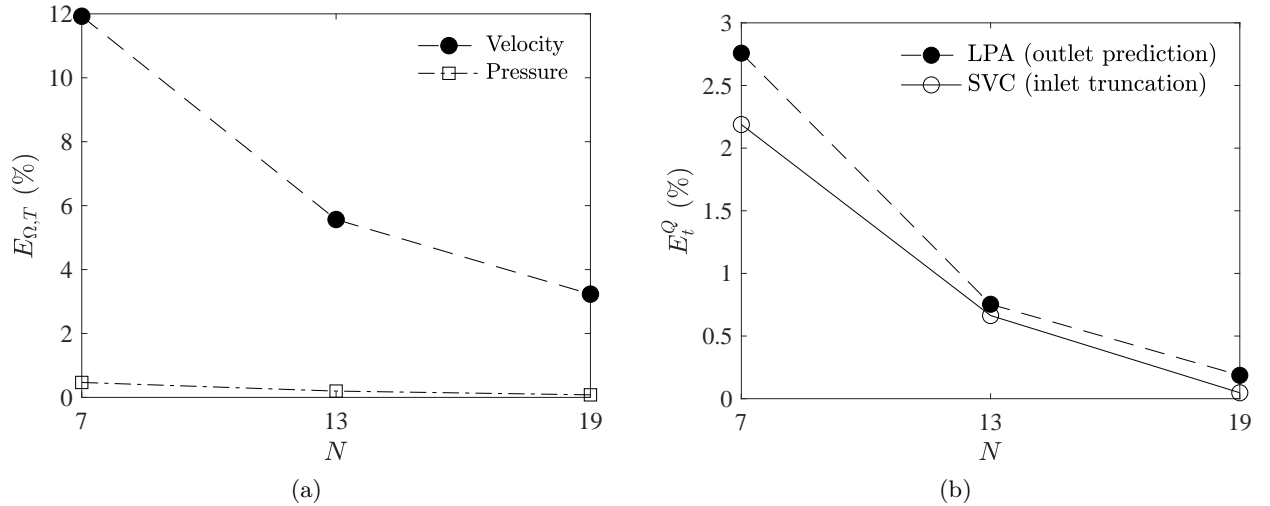


Figure 7: Pulmonary flow relative root mean square error for (a) the velocity and pressure integrated over the fluid domain and one cardiac cycle and (b) the inlet SVC flow rate (truncation) and the LPA outlet flow rate (prediction).

It is important to note that the relative error,  $E_{\Omega,T}$ , is calculated at each node within the computational domain and integrated over both space and time. This aggregate nature of the error calculation causes it to serve as an estimate for the entire solution field. However, in practice, the parameters of physiological significance are often summarized values at specific locations, such as flow rates at the outlets. For instance,

for patients who underwent the Glenn operation, the flow rate to each side of the pulmonary artery is a critical indicator for potential asymmetric lung development [79, 80]. Figure 8 shows the flow rate over one cardiac cycle for the left pulmonary artery (LPA),  $Q_{LPA}$ . This value is obtained by integrating the velocity normal to the LPA outlet surface. Notably, the flow profiles derived from the harmonic balance results closely resemble those from the conventional time results, even in the simulation using only seven time points ( $N = 7$ ). We can compute the relative error of the LPA flow rate and compare it with the inlet SVC flow rate truncation. As demonstrated in Figure 7b, the inlet truncation error provides an excellent estimate of the solution error for the LPA flow rate. Specifically, the error is less than 3% when  $N = 7$  and drops well below 1% when the number of time points exceeds  $N = 13$ .

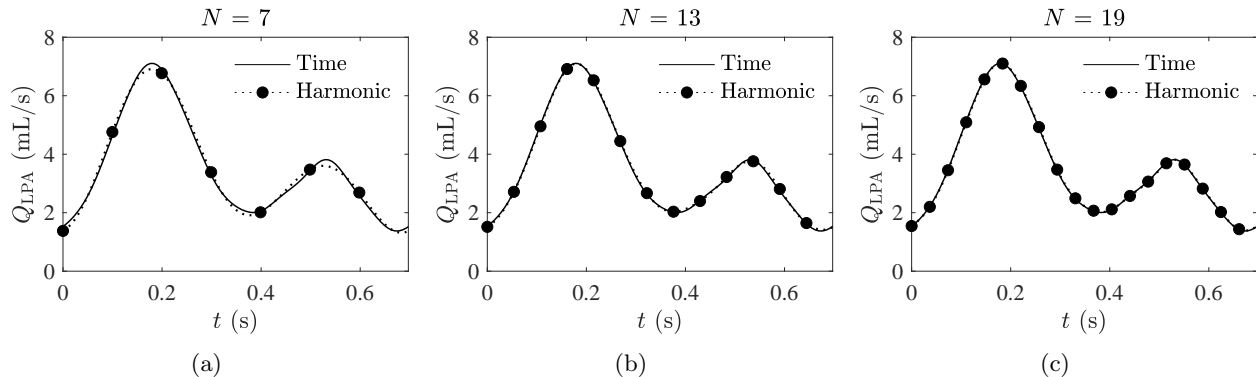


Figure 8: Left pulmonary artery (LPA) flow rate results obtained with the harmonic balance solver (solid circles) and the with the conventional time solver (solid line). The dotted line represents the reconstructed profile from the harmonic balance time points. (a)  $N = 7$ , (b)  $N = 13$ , (c)  $N = 19$ .

### 3.2 Cerebral flow

The second case presented in the study examines blood flow in the cerebral arteries, which supply approximately 20% of the brain's blood. The geometry includes two vertebral arteries (VA) inlets that converge into the basilar artery, as shown in Figure 9. This geometry was previously used in conventional computational fluid dynamics (CFD) simulations to analyze the mixing of flows from each side of the vertebral arteries [81]. The inlet flow rate profile mirrors that of the previous study, with a period of 1 second. The outlet pressure is set to the average value reported in the prior study at 115 mmHg [81]. The peak Reynolds number for this flow is approximately 120. Unlike the simpler pulmonary flow, the inflow profile for cerebral circulation is more complex and requires additional time points for accurate representation. In fact, the Fourier frequency content of the inflow includes exactly 10 unique non-zero values. Therefore, the inflow profile can be exactly represented with  $N = 19$  numbers of time points.

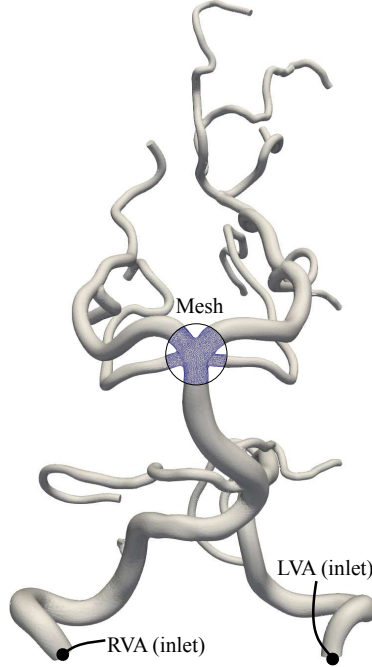


Figure 9: Clinically obtained cerebral arteries geometry used in this study with a sectional view of the mesh resolution. LVA, left vertebral artery; RVA, left vertebral artery.

Four simulations are performed: one using the conventional time-stepping solver and three using the harmonic balance solver with different numbers of time points ( $N = 7, 13,$  and  $19$ ). Figure 10 presents the harmonic balance boundary conditions. These flow profiles were prescribed identically at both the LVA and the RVA inlets. The geometry is discretized using 734,863 tetrahedral elements. The pseudo time step size is  $2 \times 10^{-2}$  resulting in a CFL number of  $C_{CFL} = 2$ .

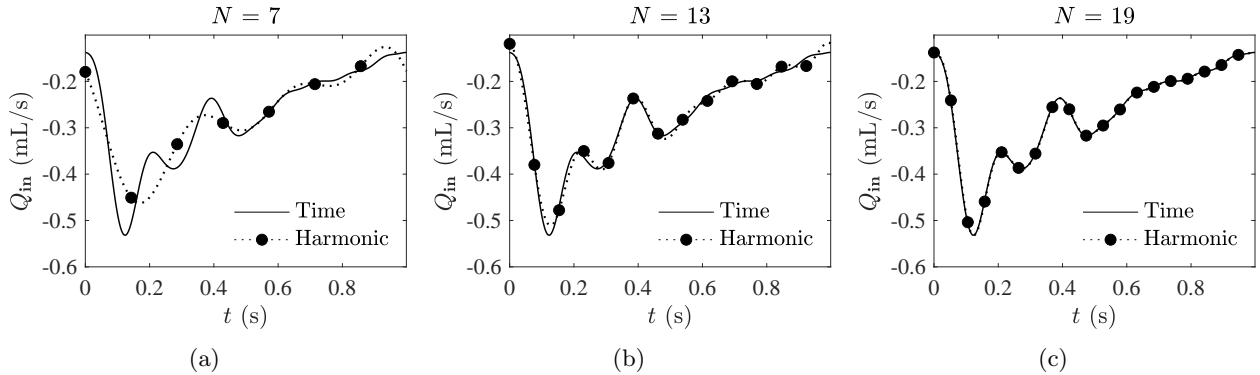


Figure 10: Discretized harmonic balance boundary conditions at each time point (black circle) on the LVA and RVA inlets. The dotted line represents the reconstructed profile from the time points. For reference, the solid line is the original flow profile in time. (a)  $N = 7$ , (b)  $N = 13$ , (c)  $N = 19$ .

Each simulation was run with 288 CPU cores at a 2.4 GHz clock rate. The simulation cost of the harmonic balance solver is shown in Figure 11. The conventional time simulation took 12 hours to run four cardiac cycles using 1000 time steps per cycle. The cases with  $N = 3$  and 25 are simulated for demonstrating the cost scaling. The cost scaling skews toward  $O(N \log(N))$  as the number of time points,  $N$ , gets larger, which is as expected from the fast Fourier transforms implementation of the harmonic balance solver.

The pressure and velocity contours for the harmonic balance solution using  $N = 19$  and the conventional time solution at  $t = 0.2s$  in the cardiac cycle are shown in Figure 12. As shown in the figure, the results



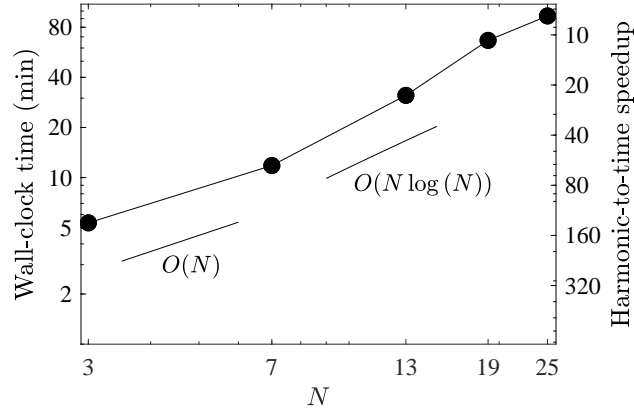


Figure 11: The cost performance of the harmonic balance solver for the cerebral flow case. The left axis shows the wall-clock time of the harmonic balance simulations. The right axis shows the speedup of the harmonic balance simulations compared to the conventional time simulation.

show no noticeable qualitative differences.

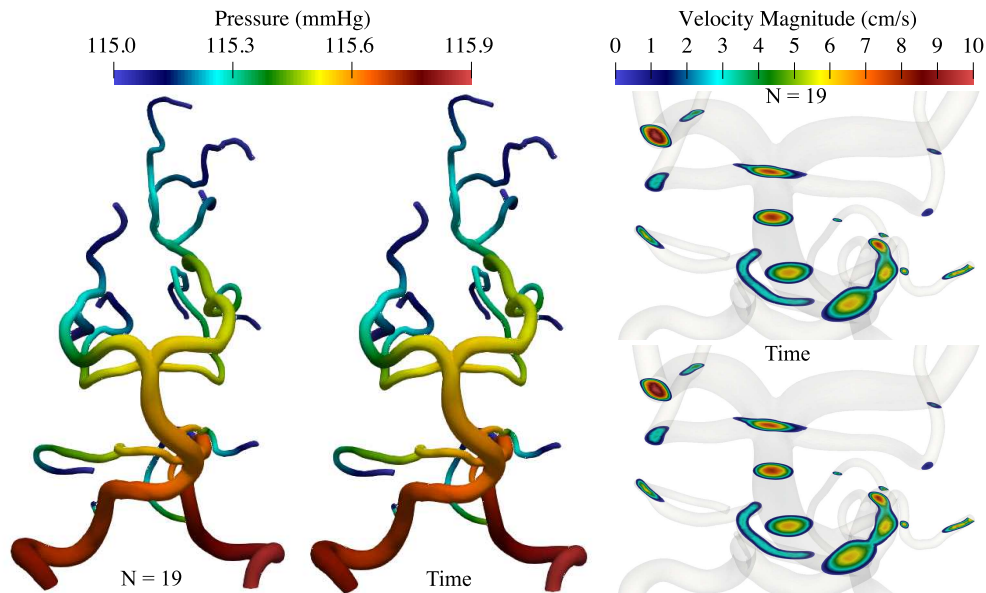


Figure 12: Harmonic balance results using  $N = 19$  compared to the conventional time results for the pulmonary flow case. The pressure and velocity magnitude contours are taken at  $t = 0.2$  seconds of the cardiac cycle.

Similar to the pulmonary flow case, we can calculate the integral relative errors. Figure 13 presents the spacial integral relative error. The error obtained using 19 time points is well under 5% at any point of the cardiac cycle. Figure 14 shows the spacial and time integral error of the solution along with the truncation error for the inlet boundary condition. In this case, due to the low Reynolds number, the inlet flow truncation error is a good indicator of the velocity field solution error. The pressure error is considerably small, owing to the large fixed pressure boundary conditions at the outlets.

Figure 14 includes an additional set of results at  $N = 25$ . Since the inlet boundary profile is exactly represented with  $N = 19$ , any simulation run using more than 19 time points will not carry an inlet truncation error. As the number of time points increases further past  $N = 19$ , the solution errors remain unchanged. This suggests that the difference between the results of the harmonic balance solver and the conventional time

solver stems within the numerical formulation itself, rather than the truncation of the solution. Determining which formulation more closely aligns with physiological results would require extensive clinical-to-simulation comparison studies, which are beyond the scope of this study.

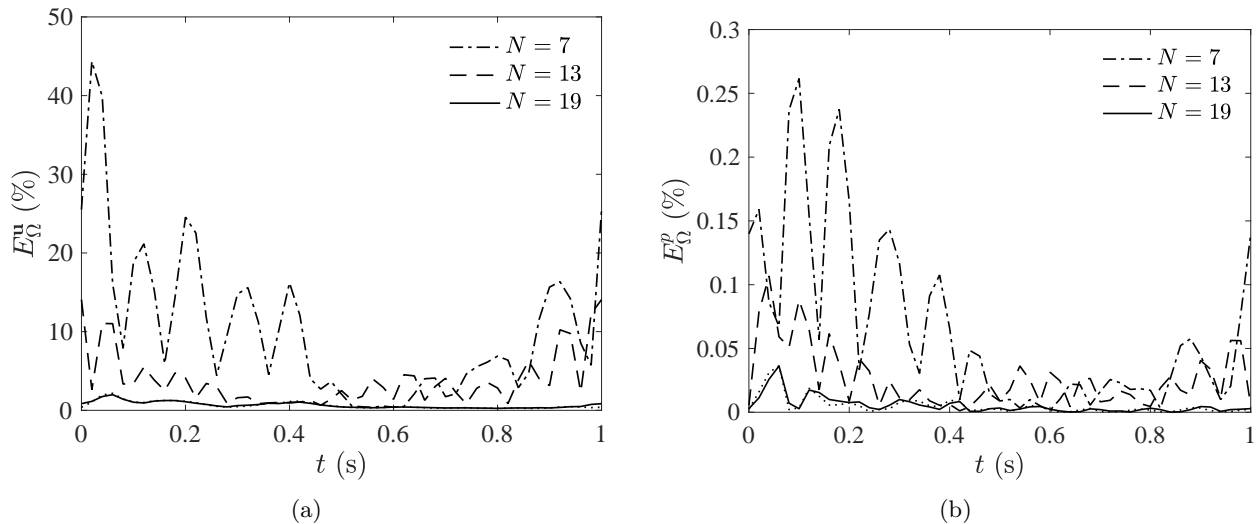


Figure 13: The volumetric integral relative root mean square error over the fluid domain for (a) the velocity vector and (b) the pressure as functions of time in the cardiac cycle of the cerebral flow.

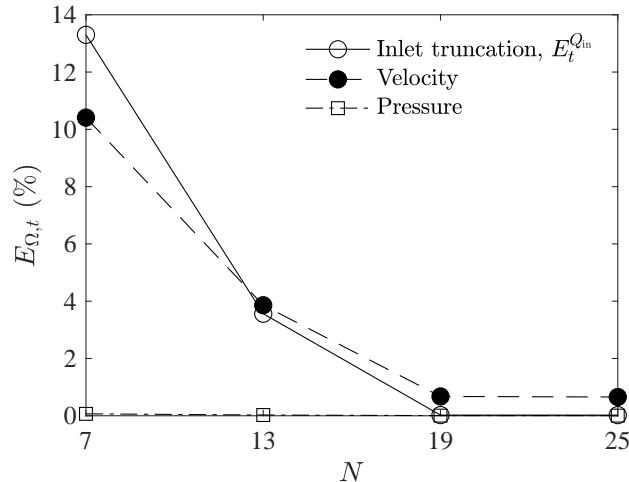


Figure 14: The volumetric and temporal integral relative root mean square error over the fluid domain and one cardiac cycle of the cerebral flow results.

### 3.3 Left main coronary arteries flow

Coronary artery disease is the leading cause of death in the United States [82, 83]. It is predominantly caused by atherosclerosis of coronary arteries, leading to narrowing or blockage of the blood supply to the heart. In the final case of this study, we will evaluate the proposed harmonic balance solver using a left main coronary arteries (LMCA) flow case. The LMCA originates from the ascending aorta and supplies blood to the left side of the heart, including the left ventricle. Computational fluid dynamics (CFD) simulations have been employed as a noninvasive method to gather flow rate and pressure information on patient-specific coronary geometries. This information can help determine the severity of coronary artery disease and assist

in surgical decision-making. The LMCA geometry used in this case was segmented from a clinically obtained image [75]. The aorta and right coronary arteries are removed from the original geometry so that only the LMCA remains, as shown in Figure 15. This decision was made due to the flow instabilities and backflow introduced by the short aorta in the original image, which made simulation convergence impossible for both the conventional CFD solver and the proposed harmonic balance solver. The inlet flow profile taken from literature [84] was used as the boundary condition for prior conventional CFD studies [85]. This inlet boundary condition poses numerical challenges because the inflow profile contains distinctive kinks, which require a substantial number of time points to represent accurately using the harmonic balance solver. However, we will demonstrate that the solver produces reasonable solutions using a manageable number of time points. The Neumann outlets are set at a steady pressure of 70 mmHg. The resulting peak Reynolds number of the domain is around 100.

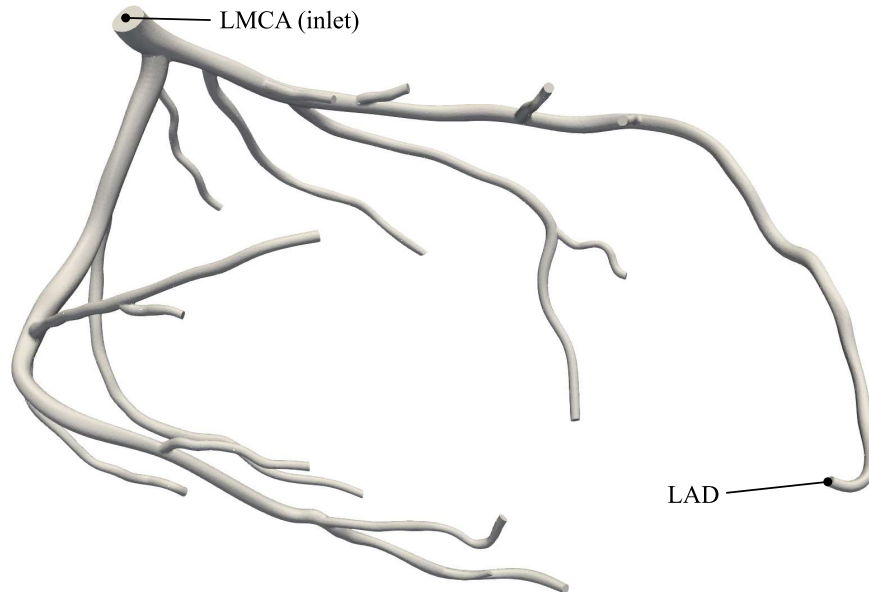


Figure 15: Clinically obtained left main coronary arteries (LMCA) geometry used in this study. The left anterior descending artery (LAD) is marked as the location for results in Figure ??.

Six simulations were performed, one using the conventional time solver and five using the harmonic balance solver ( $N = 1, 7, 13, 19,$  and  $25$ ). We simulated a case using the steady-state assumption ( $N = 1$ ) to demonstrate that this assumption, often used to reduce computational costs in clinical settings, is insufficient for capturing the full dynamics of the flow. The inlet boundary conditions for  $N = 13, 19,$  and  $25$  are shown in Figure 16. The period of the cardiac cycle is  $T = 0.8$  seconds. As observed, the sharp changes in the flow rate profile cannot be fully captured by 13 time points. As the number of time points increases, the inflow profile is more accurately represented. The computational domain is discretized using 1,336,207 tetrahedral elements. The pseudo time step size is  $5 \times 10^{-3}$ , which results in a CFL number of  $C_{\text{CFL}} = 1.3$ .

Each simulations is performed on using 288 cores at 2.4 GHz clock speed. The simulation wall clock time and speedup of the harmonic balance solver are summarized in Figure 17. The conventional time simulation took 30.3 hours to run for 4 cardiac cycles, using 800 time steps per cycle. The cost scaling is similar to that of the cerebral flow cases, going from  $O(N)$  to  $O(N \log(N))$  as  $N$  increases. The harmonic balance solver is more than 30 times faster than the conventional time solver, for the case using the largest number of time points ( $N = 25$ ).

The pressure and velocity magnitude contours for the harmonic balance solver solution using  $N = 25$  and the conventional time solver solution are shown in Figure 18. The snapshots are taken at  $t = 0.5s$  seconds in the cycle.

The spacial integral relative errors,  $E_{\Omega}$ , are presented in Figure 19 as functions of time in the cardiac cycle. Note that only  $N = 13$  and 25 results are shown for graph clarity. The times in the cycle where the errors peak coincide with the times when the inlet flow profile exhibits sharp changes. Although the maxima

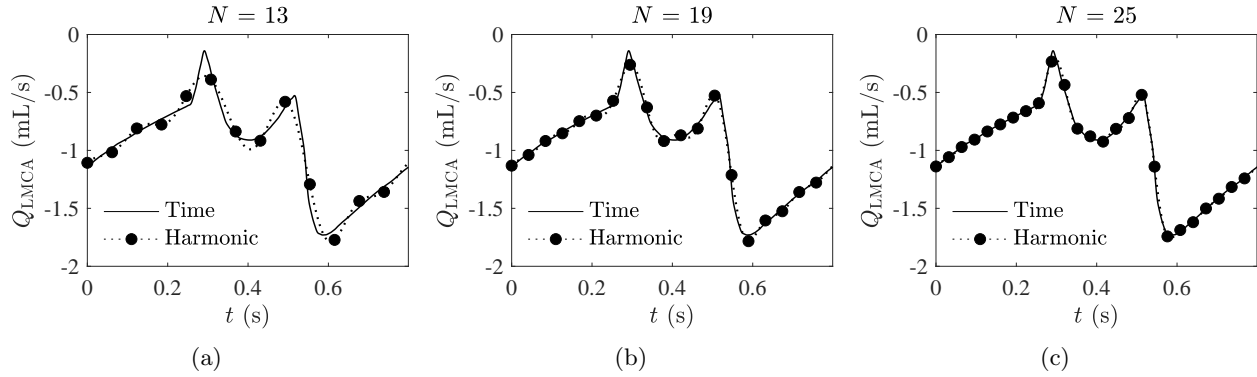


Figure 16: Discretized harmonic balance boundary conditions at each time point (black circle) on LMCA inlet. The dotted line represents the reconstructed profile from the time points. For reference, the solid line is the original flow profile

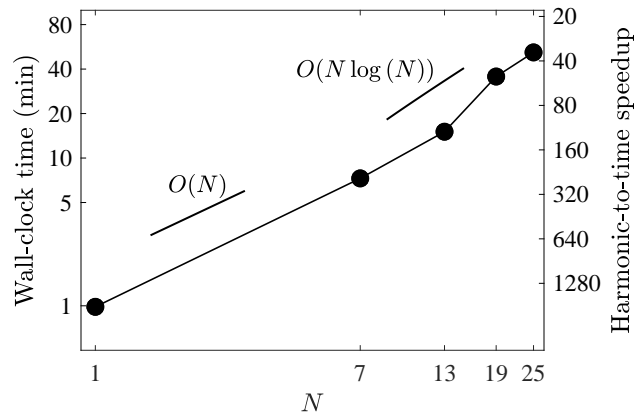


Figure 17: The cost performance of the harmonic balance solver for the coronary flow case. The left axis shows the wall-clock time of the harmonic balance simulations. The right axis shows the speedup of the harmonic balance simulations compared to the conventional time simulation.

of the error curves can be fairly large, the duration of these error spikes is short, which means that their effects are not significant to the overall solution accuracy.

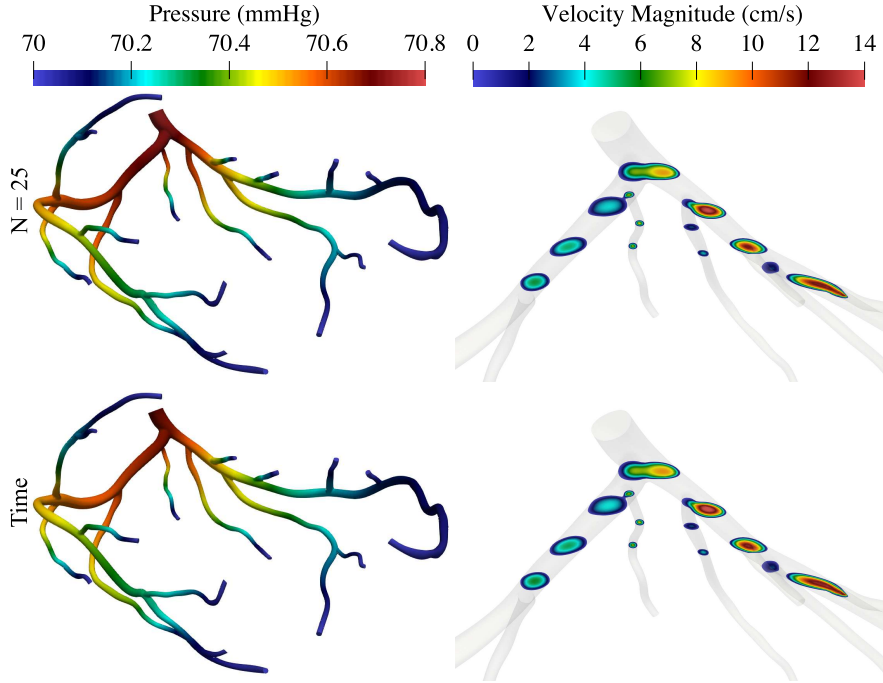


Figure 18: Harmonic balance results using  $N = 25$  compared to the conventional time results for the coronary flow case. The pressure and velocity magnitude contours are taken at  $t = 0.5$  seconds of the cardiac cycle.

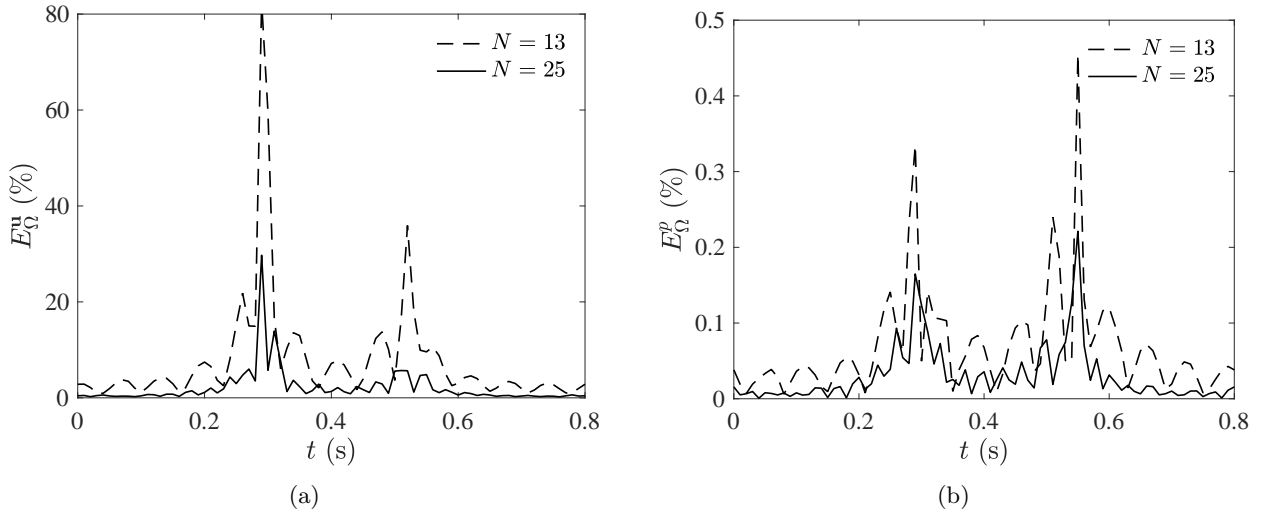


Figure 19: The volumetric integral relative root mean square error over the fluid domain for (a) the velocity vector and (b) the pressure as functions of time in the cardiac cycle of the coronary flow.

Taking both the spacial and time integral of the relative error in Figure 20a shows that the harmonic balance velocity result is within 5% of that of the conventional time solver results when  $N \geq 19$ . The steady state flow assumption ( $N = 1$ ) produces significant velocity error of more than 40%. Similar to the cerebral flow case, the inlet boundary condition truncation error is a good estimate of the overall error in the solution domain due to the flow's low Reynolds number.

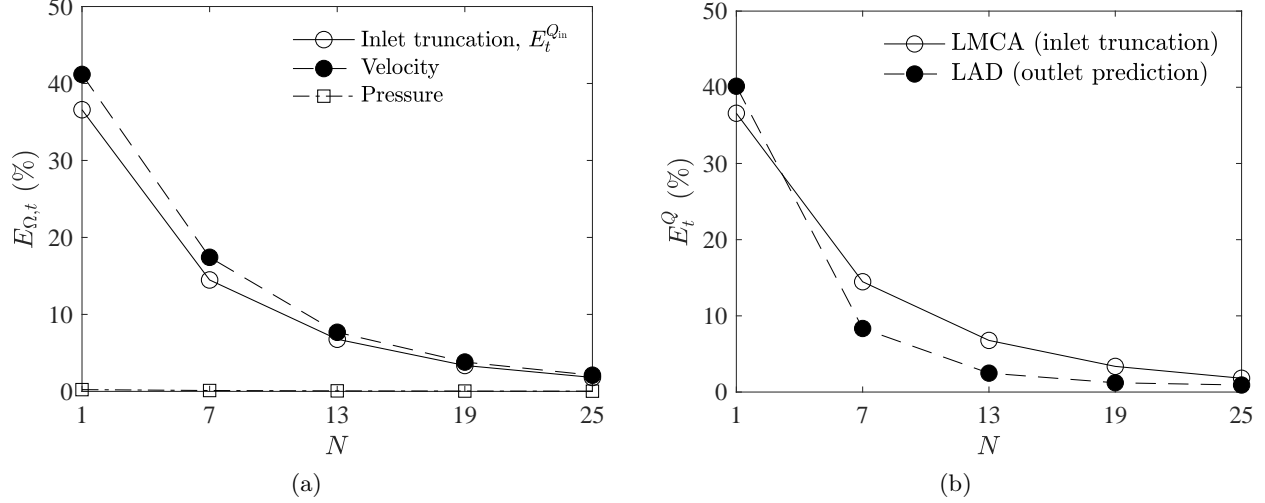


Figure 20: Left main coronary arteries flow relative root mean square error for (a) the velocity and pressure integrated over the fluid domain and one cardiac cycle and (b) the inlet LMCA flow rate (truncation) and the outlet LAD flow rate (prediction).

For some parameters of interest, the error in the results will be smaller than the inlet truncation error due to the damping effect of viscosity, which smooths out sharp changes in velocity downstream of the flow. For instance, the flow rate at the left anterior descending artery (LAD), marked in Figure 15, can be accurately predicted using just 13 time points ( $N = 13$ ), as demonstrated in Figure 21. The LAD outlet flow rate relative error is under 3% when  $N \geq 13$ . Aside from the steady flow case, the flow rate errors at the LAD outlet are significantly lower than the inlet truncation errors at the left main coronary artery (LMCA).

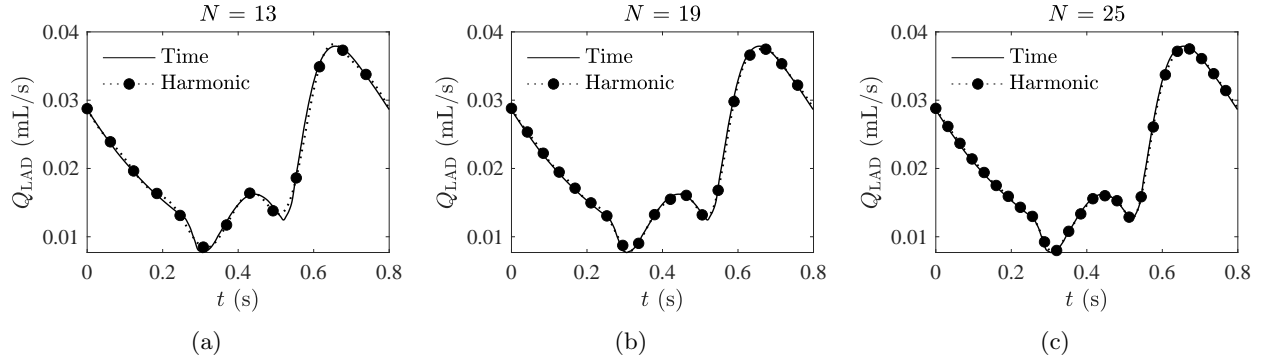


Figure 21: left anterior descending artery (LAD) flow rate results obtained with the harmonic balance solver (solid circles) and the with the conventional time solver (solid line). The dotted line represents the reconstructed profile from the harmonic balance time points. (a)  $N = 13$ , (b)  $N = 19$ , (c)  $N = 25$ .

## 4 Discussion

The above results demonstrated that the proposed harmonic balance CFD solver is a viable option for various cardiovascular simulations, providing a significant speedup over to the current time-stepping CFD solver. The requirements for conducting harmonic balance CFD simulations are close to those of conventional CFD simulations: a discretized computational domain (mesh) and boundary conditions. The harmonic balance solver has two additional prerequisites regarding the flow characteristics: 1. the flow must exhibit periodic behavior with a known frequency, which is fundamentally satisfied by cardiovascular flows, and 2. there should be no geometry-triggered instabilities or turbulence in the fluid field, meaning that the Reynolds

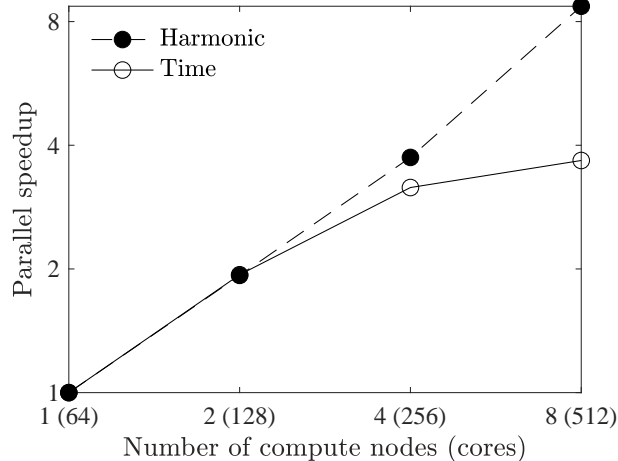


Figure 22: Strong scaling of the harmonic balance solver and the conventional time solver using the  $N = 25$  case in Section 3.3.

number has to be below the transitional flow Reynolds number, typically between 2,000 and 3,000. In cardiovascular flows, the Reynolds number can exceed this limit in the aorta, where the peak Reynolds number can reach 4,000. This is the reason why we excluded the aorta in the coronary flow case. Nonetheless, a significant portion of the human circulatory system operates within the acceptable limit, making the proposed harmonic balance solver beneficial for simulating the flow in those areas. The simplicity and adaptability of the harmonic balance CFD solver set it apart from other cost-reducing methods, such as lumped parameter networks or data-driven models, which require extensive prior training and model development to yield satisfactory results. Additionally, the harmonic balance solver is grounded in fundamental conservation laws, which other methods mentioned above do not guarantee.

In this study, the harmonic balance solver outperforms the conventional time solver by 10 to 100 times in simulation speed across all cases. This remarkable speedup is achieved by implementing a fast Fourier transform scheme for better cost scaling as the number of time points increases. The improvement in cost scaling distinguishes this study from our previous paper, where the second-order cost scaling ( $O(N^2)$ ) diminished the speedup advantage as the number of captured frequencies gets large [31]. The harmonic balance solver retains the same parallel scalability benefits as the previous study [31], which came for "free" without modifications to the solver's parallelization scheme or code structure. As shown in Figure 22, the harmonic balance simulations can be run on more parallel cores than the conventional time CFD solver while still maintaining strong scaling. This capability arises from a denser linear system at each mesh node, which results from calculating the time points simultaneously. Consequently, this higher density helps maintain strong scaling, even when fewer mesh nodes are assigned to each parallel partition as the number of cores increases.

The results from all three cases show that the truncation error from the boundary condition is a reliable indicator for the overall solution error. The number of time points ( $N$ ) chosen in the harmonic balance simulations can be determined by the acceptable level of solution error, which is reflected by the boundary condition truncation error. For simulations with intermediate Reynolds numbers around or over 1,000, additional time points are beneficial for accessing the higher-frequency flow information generated by the nonlinear convective term. It is important to emphasize that the study does not determine the actual error of the harmonic balance solver in relation to real-life physical measurement; all errors are reported relative to conventional time-stepping solvers. Our previous paper provided a comprehensive error analysis and established the bounds of the numerical errors associated with the frequency solver [31].

One potential improvement to the proposed solver is the implementation of resistance outlet boundary conditions. This boundary type is considered to be more physiologically accurate [76]. For resistance boundaries, the pressure at the boundary is proportional to that surface's flow rate. Consequently, the pressure error resulting from resistance boundaries is likely to be similar to the error of outlet flow rate. Future studies are required to confirm this hypothesis.

Potential applications of the harmonic balance solver include respiratory flow simulations, which are also periodic in time, and the peak Reynolds number is typically less than 2,000. Broadly speaking, the harmonic balance CFD solver is an excellent tool for any other application with a time-periodic flow field and low to intermediate Reynolds number flow. The use of harmonic balance CFD solver solutions to build lumped parameter networks or generate machine learning datasets can also be studied. It has the potential to significantly speed up the process of constructing and training these models. The proposed solver can also be coupled with fluid-structure interaction codes, in which the governing equations must be formulated in the harmonic balance form.

## References

- [1] Charles A Taylor, Thomas JR Hughes, and Christopher K Zarins. Finite element modeling of three-dimensional pulsatile flow in the abdominal aorta: relevance to atherosclerosis. *Annals of biomedical engineering*, 26:975–987, 1998.
- [2] C Alberto Figueroa, Irene E Vignon-Clementel, Kenneth E Jansen, Thomas JR Hughes, and Charles A Taylor. A coupled momentum method for modeling blood flow in three-dimensional deformable arteries. *Computer methods in applied mechanics and engineering*, 195(41-43):5685–5706, 2006.
- [3] Mahdi Esmaily Moghadam, Irene E Vignon-Clementel, Richard Figliola, Alison L Marsden, Modeling of Congenital Hearts Alliance (MOCHA) Investigators, et al. A modular numerical method for implicit 0d/3d coupling in cardiovascular finite element simulations. *Journal of Computational Physics*, 244:63–79, 2013.
- [4] Paul D Morris, Andrew Narracott, Hendrik von Tengg-Kobligk, Daniel Alejandro Silva Soto, Sarah Hsiao, Angela Lungu, Paul Evans, Neil W Bressloff, Patricia V Lawford, D Rodney Hose, et al. Computational fluid dynamics modelling in cardiovascular medicine. *Heart*, 102(1):18–28, 2016.
- [5] Luca Antiga, Marina Piccinelli, Lorenzo Botti, Bogdan Ene-Iordache, Andrea Remuzzi, and David A Steinman. An image-based modeling framework for patient-specific computational hemodynamics. *Medical & biological engineering & computing*, 46:1097–1112, 2008.
- [6] Hyun Jin Kim, IE Vignon-Clementel, JS Coogan, CA Figueroa, KE Jansen, and CA Taylor. Patient-specific modeling of blood flow and pressure in human coronary arteries. *Annals of biomedical engineering*, 38:3195–3209, 2010.
- [7] Bongjae Chung and Juan Raul Cebal. Cfd for evaluation and treatment planning of aneurysms: review of proposed clinical uses and their challenges. *Annals of biomedical engineering*, 43:122–138, 2015.
- [8] Rajat Mittal, Jung Hee Seo, Vijay Vedula, Young J Choi, Hang Liu, H Howie Huang, Saurabh Jain, Laurent Younes, Theodore Abraham, and Richard T George. Computational modeling of cardiac hemodynamics: current status and future outlook. *Journal of Computational Physics*, 305:1065–1082, 2016.
- [9] Kerem Pekkan, Brian Whited, Kirk Kanter, Shiva Sharma, Diane De Zelicourt, Kartik Sundareswaran, David Frakes, Jarek Rossignac, and Ajit P Yoganathan. Patient-specific surgical planning and hemodynamic computational fluid dynamics optimization through free-form haptic anatomy editing tool (surgem). *Medical & biological engineering & computing*, 46:1139–1152, 2008.
- [10] Mahdi Esmaily-Moghadam, Bari Murtuza, Tain-Yen Hsia, and Alison Marsden. Simulations reveal adverse hemodynamics in patients with multiple systemic to pulmonary shunts. *Journal of biomechanical engineering*, 137(3):031001, 2015.
- [11] Dongjie Jia, Byunghwan Jeon, Hyung-Bok Park, Hyuk-Jae Chang, and Lucy T Zhang. Image-based flow simulations of pre-and post-left atrial appendage closure in the left atrium. *Cardiovascular Engineering and Technology*, 10:225–241, 2019.



- [12] Mahdi Esmaily Moghadam, Francesco Migliavacca, Irene E. Vignon-Clementel, Tain-Yen Hsia, Alison L. Marsden, and Modeling of Congenital Hearts Alliance (MOCHA) Investigators. Optimization of Shunt Placement for the Norwood Surgery Using Multi-Domain Modeling. *Journal of Biomechanical Engineering*, 134(5):051002, 05 2012.
- [13] Alison L Marsden. Optimization in cardiovascular modeling. *Annual review of fluid mechanics*, 46:519–546, 2014.
- [14] Dongjie Jia and Mahdi Esmaily. Characterization of the ejector pump performance for the assisted bidirectional glenn procedure. *Fluids*, 7(1):31, 2022.
- [15] Phillip M Trusty, Timothy C Slesnick, Zhenglun Alan Wei, Jarek Rossignac, Kirk R Kanter, Mark A Fogel, and Ajit P Yoganathan. Fontan surgical planning: previous accomplishments, current challenges, and future directions. *Journal of cardiovascular translational research*, 11:133–144, 2018.
- [16] Dongjie Jia, Matthew Peroni, Tigran Khalapyan, and Mahdi Esmaily. An efficient assisted bidirectional glenn design with lowered superior vena cava pressure for stage-one single ventricle patients. *Journal of Biomechanical Engineering*, 143(7):071008, 2021.
- [17] Charles A Taylor, Timothy A Fonte, and James K Min. Computational fluid dynamics applied to cardiac computed tomography for noninvasive quantification of fractional flow reserve: scientific basis. *Journal of the American College of Cardiology*, 61(22):2233–2241, 2013.
- [18] Paul D Morris, Frans N van de Vosse, Patricia V Lawford, D Rodney Hose, and Julian P Gunn. “virtual” (computed) fractional flow reserve: current challenges and limitations. *JACC: Cardiovascular Interventions*, 8(8):1009–1017, 2015.
- [19] Roel S Driessen, Ibrahim Danad, Wijnand J Stuijzand, Pieter G Raijmakers, Stefan P Schumacher, Pepijn A Van Diemen, Jonathon A Leipsic, Juhani Knuuti, S Richard Underwood, Peter M van de Ven, et al. Comparison of coronary computed tomography angiography, fractional flow reserve, and perfusion imaging for ischemia diagnosis. *Journal of the American College of Cardiology*, 73(2):161–173, 2019.
- [20] Bhavik N Modi, Sethuraman Sankaran, Hyun Jin Kim, Howard Ellis, Campbell Rogers, Charles A Taylor, Ronak Rajani, and Divaka Perera. Predicting the physiological effect of revascularization in serially diseased coronary arteries: clinical validation of a novel ct coronary angiography–based technique. *Circulation: cardiovascular interventions*, 12(2):e007577, 2019.
- [21] Fuyou Liang and Hao Liu. A closed-loop lumped parameter computational model for human cardiovascular system. *JSME International Journal Series C Mechanical Systems, Machine Elements and Manufacturing*, 48(4):484–493, 2005.
- [22] JP Mynard, MR Davidson, DJ Penny, and JJ2946553 Smolich. A simple, versatile valve model for use in lumped parameter and one-dimensional cardiovascular models. *International Journal for Numerical Methods in Biomedical Engineering*, 28(6-7):626–641, 2012.
- [23] Mehran Mirramezani, Scott L Diamond, Harold I Litt, and Shawn C Shadden. Reduced order models for transstenotic pressure drop in the coronary arteries. *Journal of biomechanical engineering*, 141(3):031005, 2019.
- [24] Martin R Pfaller, Jonathan Pham, Aekaansh Verma, Luca Pegolotti, Nathan M Wilson, David W Parker, Weiguang Yang, and Alison L Marsden. Automated generation of 0d and 1d reduced-order models of patient-specific blood flow. *International journal for numerical methods in biomedical engineering*, 38(10):e3639, 2022.
- [25] Christian Tesche, Carlo N De Cecco, Stefan Baumann, Matthias Renker, Tindal W McLaurin, Taylor M Duguay, Richard R Bayer 2nd, Daniel H Steinberg, Katharine L Grant, Christian Canstein, et al. Coronary ct angiography–derived fractional flow reserve: machine learning algorithm versus computational fluid dynamics modeling. *Radiology*, 288(1):64–72, 2018.

- [26] Gaoyang Li, Haoran Wang, Mingzi Zhang, Simon Tupin, Aike Qiao, Youjun Liu, Makoto Ohta, and Hitomi Anzai. Prediction of 3d cardiovascular hemodynamics before and after coronary artery bypass surgery via deep learning. *Communications biology*, 4(1):99, 2021.
- [27] Erica L Schwarz, Luca Pegolotti, Martin R Pfaller, and Alison L Marsden. Beyond cfd: Emerging methodologies for predictive simulation in cardiovascular health and disease. *Biophysics Reviews*, 4(1), 2023.
- [28] Chenwei Meng, Anirban Bhattacharjee, and Mahdi Esmaily. A scalable spectral stokes solver for simulation of time-periodic flows in complex geometries. *Journal of Computational Physics*, 445:110601, 2021.
- [29] Mahdi Esmaily and Dongjie Jia. A stabilized formulation for the solution of the incompressible unsteady stokes equations in the frequency domain. *Journal of Computational Physics*, 473:111736, 2023.
- [30] Mahdi Esmaily and Dongjie Jia. An augmented streamline upwind/ Petrov-galerkin method for the time-spectral convection-diffusion equation. *Journal of Computational Physics*, page 113484, 2024.
- [31] Mahdi Esmaily and Dongjie Jia. A new stabilized time-spectral finite element solver for fast simulation of blood flow. *Computer Methods in Applied Mechanics and Engineering*, 425:116939, 2024.
- [32] FN Van de Vosse, J De Hart, CHGA Van Oijen, D Bessems, TWM Gunther, A Segal, BJBM Wolters, JMA Stijnen, and FPT Baaijens. Finite-element-based computational methods for cardiovascular fluid-structure interaction. *Journal of engineering mathematics*, 47:335–368, 2003.
- [33] Yuri Bazilevs, M-C Hsu, David J Benson, Sethu Sankaran, and Alison L Marsden. Computational fluid-structure interaction: methods and application to a total cavopulmonary connection. *Computational Mechanics*, 45:77–89, 2009.
- [34] Alfio Quarteroni, Alessandro Veneziani, and Christian Vergara. Geometric multiscale modeling of the cardiovascular system, between theory and practice. *Computer Methods in Applied Mechanics and Engineering*, 302:193–252, 2016.
- [35] David Kamensky, Ming-Chen Hsu, Yue Yu, John A Evans, Michael S Sacks, and Thomas JR Hughes. Immersogeometric cardiovascular fluid-structure interaction analysis with divergence-conforming b-splines. *Computer methods in applied mechanics and engineering*, 314:408–472, 2017.
- [36] Tony J. Roupheal. Chapter 4 - system nonlinearity. In Tony J. Roupheal, editor, *Wireless Receiver Architectures and Design*, pages 179–261. Academic Press, Boston, 2014.
- [37] Xuechuan Wang, Xiaokui Yue, Honghua Dai, Haoyang Feng, and Satya N. Atluri. Chapter 2 - harmonic balance method and time domain collocation method. In Xuechuan Wang, Xiaokui Yue, Honghua Dai, Haoyang Feng, and Satya N. Atluri, editors, *Computational Methods for Nonlinear Dynamical Systems*, pages 27–54. Elsevier, 2023.
- [38] A. Suarez, S. Sancho, and F. Ramirez. Chapter 3 - nonlinear analysis and design of oscillator circuits. In Antonio Raffo and Giovanni Crupi, editors, *Microwave Wireless Communications*, pages 65–133. Academic Press, 2016.
- [39] Matthew McMullen, Antony Jameson, and Juan Alonso. Acceleration of convergence to a periodic steady state in turbomachinery flows. In *39th aerospace sciences meeting and exhibit*, page 152, 2001.
- [40] Antony Jameson, J Alonso, and M McMullen. Application of a non-linear frequency domain solver to the euler and navier-stokes equations. In *40th AIAA aerospace sciences meeting & exhibit*, page 120, 2002.
- [41] Arathi Gopinath, Edwin van der Weide, Juan Alonso, Antony Jameson, Kivanc Ekici, and Kenneth Hall. Three-dimensional unsteady multi-stage turbomachinery simulations using the harmonic balance technique. In *45th AIAA Aerospace Sciences Meeting and Exhibit*, page 892, 2007.

- [42] Frederic Sicot, Guillaume Dufour, and Nicolas Gourdain. A time-domain harmonic balance method for rotor/stator interactions. *J. Turbomach.*, 134(1):011001, 2012.
- [43] Kenneth C Hall, Kivanc Ekici, Jeffrey P Thomas, and Earl H Dowell. Harmonic balance methods applied to computational fluid dynamics problems. *International Journal of Computational Fluid Dynamics*, 27(2):52–67, 2013.
- [44] Peter Arbenz, Daniel Hupp, and Dominik Obrist. Comparison of parallel time-periodic Navier-Stokes solvers. In *International Conference on Parallel Processing and Applied Mathematics*, pages 57–67. Springer, 2017.
- [45] Daniel Hupp, Peter Arbenz, and Dominik Obrist. A parallel Navier–Stokes solver using spectral discretisation in time. *International journal of computational fluid dynamics*, 30(7-10):489–494, 2016.
- [46] Taha Sabri Koltukluoğlu, Gregor Cvijetić, and Ralf Hiptmair. Harmonic balance techniques in cardiovascular fluid mechanics. In *International Conference on Medical Image Computing and Computer-Assisted Intervention*, pages 486–494. Springer, 2019.
- [47] Kenneth C Hall, Jeffrey P Thomas, and William S Clark. Computation of unsteady nonlinear flows in cascades using a harmonic balance technique. *AIAA journal*, 40(5):879–886, 2002.
- [48] I.E. Vignon-Clementel, C.A. Figueroa, K.E. Jansen, and C.A. Taylor. Outflow boundary conditions for three-dimensional simulations of non-periodic blood flow and pressure fields in deformable arteries. *Computer Methods in Biomechanics and Biomedical Engineering*, 13(5):625–640, 2010.
- [49] Y. Bazilevs, J.R. Gohean, T.J.R. Hughes, R.D. Moser, and Y. Zhang. Patient-specific isogeometric fluid-structure interaction analysis of thoracic aortic blood flow due to implantation of the Jarvik 2000 left ventricular assist device. *Computer Methods in Applied Mechanics and Engineering*, 198(45-46):3534–3550, 2009.
- [50] Thomas JR Hughes. Recent progress in the development and understanding of SUPG methods with special reference to the compressible Euler and Navier-Stokes equations. *International journal for numerical methods in fluids*, 7(11):1261–1275, 1987.
- [51] Ramon Codina. Stabilization of incompressibility and convection through orthogonal sub-scales in finite element methods. *Computer methods in applied mechanics and engineering*, 190(13-14):1579–1599, 2000.
- [52] Thomas JR Hughes, Guglielmo Scovazzi, and Tayfun E Tezduyar. Stabilized methods for compressible flows. *Journal of Scientific Computing*, 43:343–368, 2010.
- [53] Thomas JR Hughes. A multidimensional upwind scheme with no crosswind diffusion. *Finite element methods for convection dominated flows*, AMD 34, 1979.
- [54] Alexander N Brooks and Thomas JR Hughes. Streamline upwind/Petrov-Galerkin formulations for convection dominated flows with particular emphasis on the incompressible Navier-Stokes equations. *Computer methods in applied mechanics and engineering*, 32(1-3):199–259, 1982.
- [55] Tayfun E Tezduyar and Yasuo Osawa. Finite element stabilization parameters computed from element matrices and vectors. *Computer Methods in Applied Mechanics and Engineering*, 190(3-4):411–430, 2000.
- [56] M-C Hsu, Yuri Bazilevs, Victor M Calo, Tayfun E Tezduyar, and TJR2581346 Hughes. Improving stability of stabilized and multiscale formulations in flow simulations at small time steps. *Computer Methods in Applied Mechanics and Engineering*, 199(13-16):828–840, 2010.
- [57] Kenji Takizawa, Tayfun E Tezduyar, and Yuto Otoguro. Stabilization and discontinuity-capturing parameters for space–time flow computations with finite element and isogeometric discretizations. *Computational Mechanics*, 62:1169–1186, 2018.

- [58] Xuguang Wang, Monu Jaiswal, Ashton M Corpuz, Shashwot Paudel, Aditya Balu, Adarsh Krishnamurthy, Jinhui Yan, and Ming-Chen Hsu. Photogrammetry-based computational fluid dynamics. *Computer Methods in Applied Mechanics and Engineering*, 417:116311, 2023.
- [59] Thomas JR Hughes and Michel Mallet. A new finite element formulation for computational fluid dynamics: III. the generalized streamline operator for multidimensional advective-diffusive systems. *Computer methods in applied mechanics and engineering*, 58(3):305–328, 1986.
- [60] Farzin Shakib, Thomas JR Hughes, and Zdeněk Johan. A new finite element formulation for computational fluid dynamics: X. the compressible Euler and Navier-Stokes equations. *Computer Methods in Applied Mechanics and Engineering*, 89(1-3):141–219, 1991.
- [61] Yuri Bazilevs, Victor M Calo, John A Cottrell, Thomas JR Hughes, Alessandro Reali, and G23614751169 Scovazzi. Variational multiscale residual-based turbulence modeling for large eddy simulation of incompressible flows. *Computer methods in applied mechanics and engineering*, 197(1-4):173–201, 2007.
- [62] I Akkerman, Y Bazilevs, VM Calo, TJR Hughes, and S Hulshoff. The role of continuity in residual-based variational multiscale modeling of turbulence. *Computational Mechanics*, 41:371–378, 2008.
- [63] Dongjie Jia and Mahdi Esmaily. A time-consistent stabilized finite element method for fluids with applications to hemodynamics. *Scientific Reports*, 13(1):19120, 2023.
- [64] Matteo Frigo and Steven G Johnson. The design and implementation of fftw3. *Proceedings of the IEEE*, 93(2):216–231, 2005.
- [65] Kenneth E Jansen, Christian H Whiting, and Gregory M Hulbert. A generalized- $\alpha$  method for integrating the filtered Navier–Stokes equations with a stabilized finite element method. *Computer methods in applied mechanics and engineering*, 190(3-4):305–319, 2000.
- [66] Mahdi Esmaily, Yuri Bazilevs, Tain-Yen Hsia, Irene Vignon-Clementel, and Alison Marsden. A comparison of outlet boundary treatments for prevention of backflow divergence with relevance to blood flow simulations. *Computational Mechanics*, 48(3):277–291, 2011.
- [67] Mahdi Esmaily-Moghadam, Yuri Bazilevs, and Alison L Marsden. A new preconditioning technique for implicitly coupled multidomain simulations with applications to hemodynamics. *Computational Mechanics*, 52:1141–1152, 2013.
- [68] Youcef Saad and Martin H Schultz. Gmres: A generalized minimal residual algorithm for solving nonsymmetric linear systems. *SIAM Journal on scientific and statistical computing*, 7(3):856–869, 1986.
- [69] Mahdi Esmaily-Moghadam, Yuri Bazilevs, and Alison L Marsden. A bi-partitioned iterative algorithm for solving linear systems arising from incompressible flow problems. *Computer Methods in Applied Mechanics and Engineering*, 286:40–62, 2015.
- [70] David A Steinman, Yiemeng Hoi, Paul Fahy, Liam Morris, Michael T Walsh, Nicolas Aristokleous, Andreas S Anayiotos, Yannis Papaharilaou, Amirhossein Arzani, Shawn C Shadden, et al. Variability of computational fluid dynamics solutions for pressure and flow in a giant aneurysm: the asme 2012 summer bioengineering conference cfd challenge. *Journal of biomechanical engineering*, 135(2):021016, 2013.
- [71] Mahdi Esmaily-Moghadam, Tain-Yen Hsia, Alison L Marsden, Modeling of Congenital Hearts Alliance (MOCHA) Investigators, et al. The assisted bidirectional glenn: a novel surgical approach for first-stage single-ventricle heart palliation. *The Journal of thoracic and cardiovascular surgery*, 149(3):699–705, 2015.
- [72] Mahdi Esmaily-Moghadam, Yuri Bazilevs, and Alison Marsden. Low entropy data mapping for sparse iterative linear solvers. In *Proceedings of the conference on extreme science and engineering discovery environment: gateway to discovery*, pages 1–4, 2013.

- [73] M Esmaily-Moghadam, Yuri Bazilevs, and AL3294994 Marsden. Impact of data distribution on the parallel performance of iterative linear solvers with emphasis on cfd of incompressible flows. *Computational Mechanics*, 55:93–103, 2015.
- [74] George Karypis and Vipin Kumar. MeTis: Unstructured Graph Partitioning and Sparse Matrix Ordering System, Version 4.0. <http://www.cs.umn.edu/~metis>, 2009.
- [75] Nathan M Wilson, Ana K Ortiz, and Allison B Johnson. The vascular model repository: a public resource of medical imaging data and blood flow simulation results. *Journal of medical devices*, 7(4):040923, 2013.
- [76] G. Troianowski, C. A. Taylor, J. A. Feinstein, and I. E. Vignon-Clementel. Three-Dimensional Simulations in Glenn Patients: Clinically Based Boundary Conditions, Hemodynamic Results and Sensitivity to Input Data. *Journal of Biomechanical Engineering*, 133(11):111006, 12 2011.
- [77] Richard D Mainwaring, John J Lamberti, Karen Uzark, Robert L Spicer, Mark W Cocalis, and John W Moore. Effect of accessory pulmonary blood flow on survival after the bidirectional glenn procedure. *Circulation*, 100(suppl\_2):II-151, 1999.
- [78] Ara K Pridjian, Alan M Mendelsohn, Flavian M Lupinetti, Robert H Beekman III, Macdonald Dick II, Gerald Serwer, and Edward L Bove. Usefulness of the bidirectional glenn procedure as staged reconstruction for the functional single ventricle. *The American journal of cardiology*, 71(11):959–962, 1993.
- [79] ALAIN Cloutier, JUDITH M Ash, JEFFREY F Smallhorn, WG Williams, GA Trusler, RD Rowe, and M Rabinovitch. Abnormal distribution of pulmonary blood flow after the glenn shunt or fontan procedure: risk of development of arteriovenous fistulae. *Circulation*, 72(3):471–479, 1985.
- [80] Alan M Mendelsohn, Edward L Bove, Flavian M Lupinetti, Dennis C Crowley, Thomas R Lloyd, and Robert H Beekman III. Central pulmonary artery growth patterns after the bidirectional glenn procedure. *The Journal of thoracic and cardiovascular surgery*, 107(5):1284–1290, 1994.
- [81] Matthew D Bockman, Akash P Kansagra, Shawn C Shadden, Eric C Wong, and Alison L Marsden. Fluid mechanics of mixing in the vertebrobasilar system: comparison of simulation and mri. *Cardiovascular Engineering and Technology*, 3:450–461, 2012.
- [82] Chunli Shao, Jingjia Wang, Jian Tian, and Yi-da Tang. Coronary artery disease: from mechanism to clinical practice. *Coronary Artery Disease: Therapeutics and Drug Discovery*, pages 1–36, 2020.
- [83] Peter Libby and Pierre Theroux. Pathophysiology of coronary artery disease. *Circulation*, 111(25):3481–3488, 2005.
- [84] R.M. Berne and M.N. Levy. *Cardiovascular Physiology*. Mosby physiology monograph series. Mosby, 2001.
- [85] Ufuk Olgac, Dimos Poulidakos, Stefan C Saur, Hatem Alkadhi, and Vartan Kurtcuoglu. Patient-specific three-dimensional simulation of ldl accumulation in a human left coronary artery in its healthy and atherosclerotic states. *American Journal of Physiology-Heart and Circulatory Physiology*, 296(6):H1969–H1982, 2009.